Absence of a strong, deep-reaching Antarctic Circumpolar Current zonal flow across the Tasmanian gateway during the Oligocene to early Miocene

Dimitris Evangelinos, Carlota Escutia, Tina van de Flierdt, Luis Valero, José-Abel Flores, David M. Harwood, Frida S. Hoem, Peter Bijl, Johan Etourneau, Katharina Kreissig, et al.

Absence of a strong, deep-reaching Antarctic Circumpolar Current zonal flow across the Tasmanian Gateway during the Oligocene to early Miocene.

Dimitris Evangelinos[a,b], Carlota Escutia[b], Tina van de Flierdt[c], Luis Valero[d], José-Abel Flores[e], David M. Harwood[f], Frida S. Hoem[g], Peter Bijl[g], Johan Etourneau[a,h], Katharina Kreissig[c], Katrina Nilsson-Kerr[i], Liam Holder[c], Adrián López-Quirós[j,b] and Ariadna Salabarnada[b].

[a] UMR 5805 EPOC CNRS, University of Bordeaux, Bordeaux, France.

[b] Instituto Andaluz de Ciencias de la Tierra, CSIC-Univ. de Granada, Av. de las Palmeras, 4, 18100, Armilla, Spain

[c] Department of Earth Sciences and Engineering, South Kensington Campus, London SW7 2AZ, United Kingdom.

[d] Département des Sciences de la Terre, Université de Genève, Rue des Maraîchers 13, 1205 Geneva, Switzerland.

[e] Department of Geology, University of Salamanca, 37008, Salamanca, Spain.

[f] Earth & Atmospheric Sciences, University of Nebraska, Lincoln, Lincoln, NE, USA.

[g] Palaeoecology, Institute of Environmental Biology, Faculty of Science, Laboratory of Palaeobotany and Palynology, Utrecht, University, Budapestlann, 4, 3584 CD, Utrecht, The Netherlands.

[h] EPHE, PSL University, Paris, France.

[i] School of Environment, Earth and Ecosystem Sciences, Faculty of Science, Technology, Engineering and Mathematics, The Open University, Milton, Keynes, United Kingdom.

[j]Department of Geoscience, Aarhus University, Høegh-Guldbergs Gade 2, 8000, Aarhus C, Denmark.

ABSTRACT

The vigorous eastward flow of the Antarctic Circumpolar Current (ACC) connects all major ocean basins and plays a prominent role in the transport of heat, carbon and nutrients around the globe. However, the establishment of a deep circumpolar flow, similar to the present-day ACC, remains controversial thereby obscuring our

understanding of its climatic impact. Deciphering the chemical composition of Circumpolar Deep Water (CDW) within the ACC can provide critical insights about its development and evolution. Here we present new fossil fish teeth/bone debris neodymium isotope (ε_{Nd}) records from Deep Sea Drilling Project (DSDP) Sites 278 and 274 in the southwest Pacific Ocean, with the aim to trace changes in deep water masses across the Tasmanian Gateway between the early Oligocene and early Miocene (~ 33-22 Ma). Site 274 provides the first Nd isotope record proximal to the Ross Sea during the Oligocene (33.5-23.4 Ma). Its Nd isotope composition shows excursions to very radiogenic values, $\varepsilon_{Nd(t)}$ = -3.1 and $\varepsilon_{Nd(t)=}$ -3.7, at 33.5 Ma and 23.8 Ma, respectively, in response to major steps in Antarctic ice sheet expansion. A shift to lower, more unradiogenic $\varepsilon_{Nd(t)}$ values between 29.7 and 29.1Ma is linked to an increased influence of proto-CDW upwelling at the site. In contrast, the Nd isotope record from Site 278 in the southern Emerald Basin shows little variability ($\varepsilon_{Nd(t)}$= -6.0 to -6.7) throughout the Oligocene and early Miocene (30.9-21.8 Ma). Comparison with published data north of the ACC path, demonstrates the presence of two deep water masses in the South Pacific prior to the inferred onset of the ACC (33-30 Ma), one occupying depths between ~2500 and 3000 m ($\varepsilon_{Nd(t)=}$ ~-3 to -5) and a deep/bottom water mass (> 3000 m) with a more unradiogenic Nd isotope composition ($\varepsilon_{Nd(t)=}$ ~ -6). Site 278 located close to the proto-polar front (proto-PF) indicates that following the inferred onset of the ACC, deep waters bathing the southern Emerald Basin remained more radiogenic in the Southwest Pacific compared to sites along the proto-PF in the South Atlantic and Indian Ocean ($\varepsilon_{Nd(t)=}$ ~ -8.1). This indicates a provinciality in Nd isotope compositions of deep waters along the proto-PF across the Tasmanian Gateway. Our data are incompatible with the existence of a modern-like homogenous (lateral and vertical) Nd isotope composition of CDW along the main flow path of the ACC in all oceanic basins in the Oligocene to early Miocene. We attribute

distinct Nd isotope compositions of deep waters across the Tasmanian Gateway to reflect a less deep reaching and weaker ACC (proto-ACC) than today. Our findings suggest that the modern strong and deep-reaching ACC flow must have been developed at a later point in the Neogene.

***Keywords*:** ACC, CDW, neodymium isotope ratios, deep ocean circulation, Tasmanian Gateway, Oligocene-early Miocene

1. INTRODUCTION

The Antarctic Circumpolar Current (ACC) is the world´s largest and strongest ocean current, transporting ~136-162 x 10^6 m^3 s^{-1} of water along a ~20,000 km long path around Antarctica (e.g., Rintoul et al., 2014). The absence of continental barriers around 60°S permits the vigorous eastward flow of the ACC, which is driven by the strong westerly winds (westerlies) and buoyancy forcing (Rintoul, 2018). Most of the circumpolar flow of the ACC takes place along the Polar and the Subantarctic Fronts (PF and SAF, respectively), which extend from the surface to the seafloor (i.e. deep-reaching), connecting the Atlantic, Pacific and Indian Oceans, thus actively modulating the global ocean circulation (Orsi et al., 1995; Sokolov and Rintoul, 2007; Rintoul, 2018). This interbasin connection of the ACC is a critical feature of the modern global overturning circulation, which carries heat, carbon and nutrients around the globe. It modulates the exchange of heat, moisture and carbon dioxide (CO_2) between the ocean and the atmosphere and controls local and global marine primary productivity (Rintoul, 2018).

Despite the critical role of today´s strong deep-reaching ACC flow in the global ocean circulation and Earth´s climate, there is still an ongoing debate regarding the timing of its onset and evolution towards a modern-like configuration throughout the Cenozoic period. Major

changes in paleogeography and seafloor paleobathymetry related to tectonic activity through time, as well as changes in climate are likely to have controlled the initiation and evolution of the ACC during the Cenozoic. For example, it is widely accepted that the ACC only initiated after the opening of the two last major land barriers within its circum-Antarctic flow, the Drake Passage and the Tasmanian Gateway, and their respective deepening to bathyal depths (>2000 m). Dating the time when the Drake Passage reached this depth is controversial, spanning from the middle Eocene to the late Miocene (see Dalziel, 2014 for discussion). In contrast, the opening of the Tasmanian Gateway is better constrained (Stickley et al, 2004).

A Southern Ocean with closed tectonic gateways featured clockwise gyres in the South Pacific and South Indian/Atlantic Ocean basins (Huber et al., 2004). Between ~49 Ma and 35.5 Ma, a shallow current flowing westward across the Tasmanian Gateway (from the Pacific to the Indian Ocean) was proposed based on marine microfossils, organic geochemical records and model simulations (Huber et al., 2004; Bijl et al., 2013). Initial opening was followed by intensified deepening of the seaway between ~35.5 and 30.2 Ma as indicated by the analysis of sedimentological, micropaleontological and paleomagnetic data (Stickley et al., 2004). Chemical water mass reconstructions suggest a westward flowing (i.e., from the Pacific to the Indian Ocean) deep water current connecting both sides of the northern parts of the Tasmanian Gateway between 32 and 30 Ma (Scher et al., 2015). A deep eastward flowing water connection between the Indian and Pacific sectors of the Southern Ocean, was only established after 30 Ma, probably due to alignment of the northern part of the Tasmanian Gateway within the latitudinal band of the westerlies (Scher et al., 2015). However, micropaleontological and paleotemperature records suggest weak latitudinal paleotemperature gradients and warm conditions prevailed in the Southern Ocean until at least the mid-Miocene (Bijl et al., 2018; Hartman et al., 2018; Salabarnada et al., 2018; Sangiorgi et al., 2018). Thus, the characteristics of this nascent ACC remain poorly understood.

One possible way to reconstruct past connectivity along the ACC is to track the evolution of Circumpolar Deep Water (CDW), using neodymium (Nd) isotope compositions ($^{143}Nd/^{144}Nd$ ratio) of ambient seawater in fossil fish teeth and bones (e.g., Wright et al., 2018). Circumpolar Deep Water is the most voluminous water mass in the Southern Ocean, occupying the shallow to deep layers of the ACC in the Southern Ocean (Orsi et al., 1995). Today, CDW has a vertically and horizontally homogenous Nd isotope composition, probably due to the strong vertical and horizontal mixing along the frontal systems (e.g., Stichel et al., 2012; Lambelet et al., 2018). These findings indicate that the evolution of the Nd isotope composition of CDW in the past may provide important insights into interbasinal connections/circulation in the Southern Ocean.

Neodymium is incorporated into fish teeth at the sediment-water interface at the time of deposition, remineralisation and burial (Martin and Haley, 2000). Post-burial alteration is generally negligible relative to the early diagenetic rare earth element (REE) uptake, allowing retention of the Nd isotope composition of bottom water signals (e.g., Martin and Haley, 2000). Neodymium is a lithogenic element, introduced to the ocean at its interfaces with the solid earth (e.g., van Flierdt et al., 2016). Water masses forming in the different oceanic basins are distinct in their Nd isotope fingerprint, due to the distribution of geological ages and lithologies around the globe, with younger volcanogenic material yielding more radiogenic (higher) Nd isotope compositions, and older cratonic rocks being characterised by less radiogenic (lower) Nd isotope compositions. ε_{Nd} denotes the deviation of a measured $^{143}Nd/^{144}Nd$ ratio from the chondritic uniform reservoir in parts per 10,000 (Jacobsen and Wasserburg, 1980). Because seawater Nd has a relatively short residence time in the ocean (~500 to 1,000 years) (Tachikawa et al., 2003), Nd can be carried from one ocean basin to another, and hence trace the provenance of water masses.

Here we present new Oligocene to lower Miocene neodymium isotope data obtained from fossil fish teeth and bones (fish debris) in sediments recovered by the Deep Sea Drilling Project (DSDP) at Sites 278 and 274. Site 278 is strategically located within the main path of the modern ACC in the southern Emerald Basin (Kennett et al., 1975; Rintoul et al., 2014), while Site 274 is situated proximal to the Ross Sea in the Adare Basin (Figs. 1A; 1B; S1) (Hayes et al, 1975). Our new data provide critical insights into the chemical evolution of CDW in the Southwest Pacific in the time period following the initial (northern) opening of the Tasmanian Gateway and leading up to the development of the modern-like ACC.

2. Modern oceanographic setting of drill sites DSDP 274 and 278

To study the history of the ACC, and particularly the chemical composition of deep waters through the Oligocene to early Miocene, we used sediments recovered from Hole 278 (Kennett et al., 1975). Site 278 (56°33.42´S, 160°04.29´E, 3675 m water depth) is located on a pelagic contourite drift in the southern Emerald Basin (Figs. 1A; 1B) (Kennett et al., 1975). At present, the site is located close to the northern branch of the Polar Front (PF) and within the main pathway of the ACC (Sokolov and Rintoul, 2007; Rintoul et al., 2014). As the ACC enters the Southwest Pacific through the Tasmanian Gateway, its flow is constrained by the Macquarie Ridge, which extends from depths of 5000 m to an average depth of 1500 m between 47°S and 56°S (Rintoul et al., 2014). The ACC passes over and through narrow gaps of the Macquarie Ridge and south of the ridge crest around 56°S, before reaching the southern Emerald Basin (Rintoul et al., 2014). From there, the ACC flows around the southern edge of the Campbell Plateau and to the Bounty Trough, reinforcing the Deep Western Boundary Current (DWBC). South of the Bounty Trough (46°S) the ACC turns to the east and continues its journey across the South Pacific, while the DWBC continues north towards the equator in the Pacific Ocean basin (Carter and McCave 1997). The ACC carries CDW eastwards from

148 the Southeast Indian Ocean into the Southwest Pacific Ocean. In the modern southern Emerald
149 Basin, CDW extends to the seafloor, bathing Site 278 (Figs. 1B; S1-S2) (Rintoul et al., 2014;
150 Lambelet et al., 2018).

151 Site 274 (68°59.81´S, 173°25.64´E, 3305 m water depth) was drilled on the lower
152 continental rise, 250 km north-northeast of Cape Adare (Hayes et al., 1975) (Fig. 1B). It is
153 currently situated south of the Southern ACC Front (SACCF) (Figs. 1B; S1) (Sokolov and
154 Rintoul, 2007) and within the main outflow path of bottom water formed in the western Ross
155 Sea (Gordon et al., 2009). At a depth of 3305 m, the main modern water mass encountered is
156 Ross Sea Bottom Water (RSBW) (Fig. 1B; S1). Today, most of the dense shelf water on the
157 Ross Sea shelf resides in the Joides and Drygalski troughs, from where it is exported as RSBW
158 to the abyssal plains (Fig. 1B) (Gordon et al., 2009). In contrast to CDW, which can be found
159 all around Antarctica, bottom topography restricts the pathway of the Antarctic Bottom Water
160 (AABW), including RSBW, in the Southern Ocean (Orsi et al., 1995). Only a small portion of
161 RSBW formed in the western Ross Sea flows northward from its outlets, with most of it being
162 diverted westward against the continental slope into the deep Australian-Antarctic Basin
163 (Gordon et al., 2009). Through diapycnal mixing with overlying CDW, the hydrographic
164 properties of RSBW quickly erode along its westward pathway and are only detectable to
165 ~140°E along the Adélie-Wilkes Coast (Rintoul, 1998). In contrast, there is a larger fraction of
166 RSBW detected north of the Ross Sea, but this variety of RSBW forms predominantly in the
167 central Ross Sea and is channelled to the continental slope by the Glomar Challenger trough
168 and into the Hillary Canyon. Much of this bottom water enters the southeast Pacific Basin (Fig.
169 1B) (Gordon et al., 2009).

170 **FIGURE 1**

2.1 Modern Nd isotope signatures of deep and bottom waters around the Tasmanian Gateway

Globally, North Atlantic Deep Water (NADW) and Pacific Deep Water (PDW) constitute water mass endmembers in terms of their Nd isotope composition. Modern NADW is characterised by relatively negative ε_{Nd} values (ε_{Nd} ~ -12 to 13) (e.g., Lambelet et al., 2016), resulting from the weathering of old cratonic rocks surrounding the North Atlantic. Pacific Deep Water, in contrast, carries less negative (i.e. more radiogenic) ε_{Nd} values of ~ -4 (e.g., Amakawa et al., 2009), due to the influence of weathering of younger volcanogenic material around the North Pacific. Modern CDW in the Southern Ocean is characterised by a relatively homogenous Nd isotope composition along the flow path of the ACC across all ocean basins and with depth (ε_{Nd} = -8.3 ± 1.5; n = 158) (Figs. 2A) (Lambelet et al., 2018 and references therein). In the western part of the Tasmanian Gateway along the ~140°E meridian, CDW exhibits ε_{Nd} values of -8.6 ± 0.4 (n=4) around 2500-4300 m (Lambelet et al., 2018). In the eastern part of the gateway, in the Macquarie Ridge region, close to Site 278, CDW has ε_{Nd} values of -9.0 ± 0.2 and -9.2 ± 0.2 between 3201 and 4183 m, respectively (Figs. 2A; S2) (Lambelet et al., 2018). Ross Sea Bottom Water exhibits a more radiogenic Nd isotope signature than CDW, probably acquired from Ross Sea shelf sediments and mixing with shelf waters (ε_{Nd} = -6.5 to -7.5; Rickli et al., 2014; Basak et al., 2015) (Fig. 2B).

FIGURE 2

3. MATERIALS AND METHODS

3.1 Study sites, age models, and paleodepths

Our study focuses on the lower part of Hole 278 at DSDP Hole 278 (cores 34-26, 429-329 meters below sea floor (mbsf)). Sediments from this interval consist of (i) siliceous nannofossil chalk (429-386 mbsf), and (ii) detrital and nannofossil-bearing radiolarian-diatom ooze, alternating with siliceous oozes (386-329 mbsf) (Kennett et al., 1975). A new age model for the studied sections of Site 278 has been established based on the integration of new magnetostratigraphic data with revised diatom, radiolarian and calcareous nannofossil biostratigraphy, calibrated to the Geological Time Scale (GPTS) 2012 (Gradstein et al., 2012) (Fig. 3; Supplementary Text; Tables S1-S4).

For DSDP Site 274, we focus on two distinct intervals (408.5-313.5 mbsf and 199.5-180.5 mbsf). Shipboard core descriptions report that sediments between 408.5 and 328 mbsf are composed of silty claystones with local presence of chert layers. Sediments between 323 and 180.5 mbsf consist of diatom-detrital silty clay and minor silty clay diatom ooze (Hayes et al., 1975). Based on the initial age model, sediments between 408.5 and 180.5 mbsf are early to late Oligocene in age (Hayes et al., 1975). New dinocyst constraints combined with new magnetostratigraphic data and revised diatom biostratigraphy (updated from Hayes et al. (1975)) calibrated to GPTS 2012 (Gradstein et al., 2012) provide an updated age model for the studied sediments at Site 274 from ~33.7 to 23.3 Ma (Fig. S4) (Hoem et al., 2021).

We reconstructed the paleoposition of Sites 278 and 274 using the G-plates geodynamic modeling (http://www.gplates.org; Müller et al., 2018), utilizing the plate circuit of Müller et al. (2016). Paleodepths for the sites were obtained from the paleo-bathymetry grids generated by the Earthbyte group (Scotese and Wright, 2018), incorporating the reconstructed paleolocation of the two sites (Fig. S5). Our reconstructions show that Site 278 migrated northwards from ~62.84°S (~30 Ma) to 61.4°S (~23 Ma); its paleodepth varied between 3500 and4000 m throughout the Oligocene and early Miocene. Site 274 has migrated north from a position of ~70.22°S in the early Oligocene (~33 Ma) to ~69.57°S at the end of the Oligocene-

Miocene transition (~23 Ma) and remained at ~2500-3000 m water depth throughout the Oligocene.

3.2 Neodymium isotope analyses

Fish teeth and bones (hereafter termed fish debris) were handpicked from the > 63 µm sediment fractions isolated by wet sieving. A total number of 32 samples were selected for fish debris Nd isotope analyses (20 samples from Site 278 and 12 samples from Site 274) (Table S5). All samples were treated with ultraclean 18 MΩ water (Milli-Q water) and methanol to remove debris from surfaces and cavities following Martin and Haley (2000) in the MAGIC laboratories at Imperial College London (see also Huck et al., 2017). Cleaned fish debris samples were subsequently transferred into cleaned microcentrifuge tubes and dissolved overnight in 50 µL of 2M HCl. Dissolved fish debris were loaded on Biorad cation exchange resin (200-400 µm mesh) to separate the REEs from the sample matrix and Eichrom Ln-Spec resin (50-100 µm bead size) to separate Nd from the other REEs.

Furthermore, seven samples were selected (two from Site 278 and five from Site 274; Table S5) to determine the detrital Nd isotope composition in order to evaluate potential contribution of the detrital sediments to the porewaters or overlying bottom water signature. Samples were dried and gently homogenised using mortar and pestle. Approximately 500 mg of homogenised material was subjected to a carbonate leaching procedure to remove biogenic carbonate using 30 ml of 1.5% buffered acetic acid (modified from Biscaye (1965)). Due to the significant carbonate content of the samples from Site 278 (38 to 43 %), approximately 1.5 g of dried sample and 70-75 ml of 1.5% buffered acetic acid were used. Exchangeable ions were subsequently removed using 10 ml 1 M $MgCl_2$ solution. In a third step, ferromanganese oxides and oxyhydroxides were removed using a weak reductive solution of 0.005 M Hydroxylamine Hydrochloride (NH_2OH) 1.5% acetic acid and 0.03 M Na_2-EDTA for one

hour, followed by a stronger leaching step utilising 0.05 M NH_2OH for 17 hours. 50 mg of leached and water washed detrital sediment was subsequently dried, weighted and digested on a hotplate using a mixture of 1 ml of concentrated HNO_3, 0.8 ml $HClO_4$ and 2 ml HF. The detrital samples were processed using the same ion chromatography as the fish debris samples.

Neodymium isotope ratios of fish debris and detrital sediment samples were determined on a high-resolution Nu Plasma multiple collector inductively coupled plasma mass spectrometer (MC-ICP-MS) at Imperial College London, operated in static mode. Instrumental mass bias was corrected for using a $^{146}Nd/^{144}Nd$ ratio of 0.7219. All reported $^{143}Nd/^{144}Nd$ ratios are corrected to a nominal JNd_i value of 0.512115 (Tanaka et al., 2000) using bracketing standards. JNd_i standards were also used to monitor external reproducibility, and accuracy was evaluated by processing USGS BCR-2 rock standards alongside samples, which yielded average $^{143}Nd/^{144}Nd$ ratios of 0.512636 ± 0.000008 (n=23; 2s.d.), in agreement with the published BCR-2 $^{143}Nd/^{144}Nd$ ratio of 0.512638 ± 0.000015 (Weis et al., 2006) (Table S5).

3.3 Rare earth element analyses

To correct for the decay of ^{147}Sm to ^{144}Nd within the fish debris over time, we used the average Sm and Nd concentrations measured for two fish debris samples from Site 278 ($^{147}Sm/^{144}Nd$ ratios of 0.1275 and 0.1256; $^{147}Sm/^{144}Nd_{average}$ = 0.1266) and three fish debris samples from Site 274 ($^{147}Sm/^{144}Nd$ ratios of 0.1532, 0.1921, and 0.2662; $^{147}Sm/^{144}Nd_{average}$ = 0.2038). The range of Sm/Nd ratios reported here are consistent with values from Oligocene to Miocene fish debris material elsewhere (Huck et al., 2017; Wright et al., 2018; Evangelinos et al., 2020). Corrections for in situ decay of ^{147}Sm amounted to 0.19 to 0.28 ε_{Nd} units for Site 278 and 0.02 to 0.14 ε_{Nd} units for Site 274; (t) denotes age-corrected samples (Table S5).

To investigate whether the Nd in the fish debris is of authigenic nature (i.e. seawater-derived), the full suite of REE concentrations were determined on one fish debris sample from

Site 278 and three fish debris samples from Site 274 (Table S6). Rare earth element analysis was performed at the Open University using an Agilent Technologies 8800 Triple-Quad Inductively Coupled Plasma-Mass Spectrometer (ICP-MS). Analyses were standardized via a suite of seven synthetic multi-element standards made up with certified plasma standard solutions. An intermediate synthetic multi-element monitor standard, a fossil bone standard (Chavagnac et al. 2007) and a 2% HNO_3 blank were run every 5^{th} sample to monitor instrument drift and precision. Precision was generally better than ±2% (1 s.d.). Both oxide interferences (CeO^+/CeO^-) (<0.5%) and doubly charged species (Ce^{++}/Ce^+) (<1.2%) were kept low. All REE data were normalised to Post Archean Shale (PAAS) concentrations (Taylor and McLennan, 1985).

4. RESULTS

4.1 Age model DSDP Site 278

An age-depth model for the Oligocene and lower Miocene intervals of DSDP Site 278 is developed from the integration of new magnetostratigraphic data, calcareous nannofossil, marine diatom, and radiolarian biostratigraphy, calibrated using the Geological Time Scale (GPTS) 2012 (Gradstein et al., 2012) (Figs. 3; Supplementary Text; Tables S1-S4). We also present an alternate age model that fit with the constraints of the data (for details see supplementary material). The stratigraphic section cored at Site 278 from the bottom of the sedimentary section in core 34 at ~429 mbsf up to sample 278-21R-1, 50 cm at ~282 mbsf spans the time interval from ~ 31 to 17.7 Ma, with one unconformity noted between samples 278-31R-3, 35 cm and 278-31R-2, 139 cm (398.85 – 399.89 mbf), which removed a ~2.4 m.y. time interval from 28.2 to 25.8 Ma. The top of this interval is bounded by an unconformity between samples 278-21R-1, 50 cm and 278-20R-6, 50 cm (281.5 mbsf), which removed the time interval 17.6 to 15.5 Ma (Fig. 3). Studied sediments (cores 34R-26R) are dated between

289 ~31 and 21.7 Ma, similar to the initial shipboard ages (Fig. 3), suggesting upper Oligocene to
290 lower Miocene sediments (Kennett et al., 1975).

291 **FIGURE 3**

292 **4.2 Fish debris Nd isotope compositions**

293 Fish debris Nd isotope data from Site 278 show little variability, ranging from $\varepsilon_{Nd(t)}$ = -
294 6.0 ± 0.2 to 6.7 ± 0.2 from the early Oligocene to the early Miocene (~ 30.9-21.8 Ma) (Fig. 4;
295 Fig. S6A; Table S5). The average $\varepsilon_{Nd(t)}$ throughout the record is -6.4 ± 0.2 (n=20). In contrast,
296 fish debris Nd isotope data from Site 274 show more variability, and reach from maximum
297 values of -3.1 ± 0.3 at 33.5 Ma and -3.7 ± 0.3 at 23.8 Ma to relative minima of -5.0 ± 0.1, at
298 ~33.2-29.7 Ma, -6.2 ± 0 at ~29 Ma, -7.3 ± 0.3 and -6.8 ± 0.2 at ~24.3 and 24.0 Ma, respectively
299 (Fig. 4; Fig. S6B; Table S5). The late Oligocene time period features a pronounced excursion
300 to more radiogenic $\varepsilon_{Nd(t)}$ values by ~3 epsilon units between 24.0 and 23.8 Ma.

301 **4.3 Bulk sediment Nd isotope compositions**

302 The detrital samples at Site 278 exhibit $\varepsilon_{Nd(t)}$ values of -10.4 ± 0.3 (~ 30.5 Ma) and -7.9
303 ± 0.3 (~ 21.8 Ma), respectively (Fig. 4; Fig. S6A; Table S5). Lower Oligocene detrital sediment
304 Nd isotope compositions from Site 274 exhibit $\varepsilon_{Nd(t)}$ values of -4.2 ± 0.3 (~33.5 Ma), -7.6 ±
305 0.3 (~33.2 Ma) and -8.5 ± 0.3 (~29 Ma). Two additional late Oligocene detrital sediment
306 samples yielded $\varepsilon_{Nd(t)}$ values of -10.3 ± 0.3 and -8.5 ± 0.3 at ~24.0 Ma and 23.8 Ma, respectively
307 (Fig. 4; Fig. S6B; Table S5).

308 **4.4 Fish debris REE patterns**

309 Five fish debris samples from Site 278 and Site 274 yielded middle-REE enriched
310 patterns (Fig. 5; Table S6). Only one sample from section 278-33R-6 showed a negative Ce

anomaly, which together with the middle-REE enriched patterns represent a diagnostic feature of seawater-derived Nd in fish teeth samples (Scher et al., 2011).

FIGURE 4

FIGURE 5

5. DISCUSSION

5.1 Reliability of Nd isotopes from Sites 278 and 274

Results of Oligocene to Miocene-aged fish debris samples at Site 278 (paleodepth: 3500-4000 m) are more radiogenic (less negative) in their Nd isotope composition ($\varepsilon_{Nd(t)}$ = -6.0 to -6.7) than modern CDW in the south Emerald Basin (ε_{Nd} = ~ -9) at ~3200-4200 m water depth (Lambelet et al., 2018). Results for Site 274 ($\varepsilon_{Nd(t)}$ = -3.1 to -7.3) show generally more radiogenic values compared to ambient RSBW (ε_{Nd} = -6.5 to -7.5; Rickli et al., 2014; Basak et al., 2015) (Fig. 4). The first question to address is if the fish debris record a purely authigenic signal.

Site 278 is located near the Macquarie Ridge, a relict volcanic mid-ocean ridge, characterised by basalts and peridotites with an ε_{Nd} value of +7 to +11 (Dijkstra et al., 2009; Conway et al., 2012). Interaction of volcanic sediments and/or hydrothermal products with ambient seawater could have altered the ε_{Nd} values at Site 278 towards more radiogenic values. However, hydrothermal activity has been shown to be a sink rather than a source of Nd near ridges (Stichel et al., 2018). Moreover, fish teeth records from the Kerguelen Plateau show no changes in their Nd isotopic composition associated with the local volcanic activity during the timing of the northern Kerguelen Plateau emplacement (Wright et al., 2018). Volcanic glass and rock fragments have been reported from close to the base of siliceous nannofossil chalk at

Site 278 (Kennett et al., 1975) (~31-28.2 Ma, based on our new age model). However, the lack of any significant variability in our fish debris Nd record makes it difficult to reconcile any major volcanic contribution to the porewater and hence to the fish debris Nd isotope signature (Figs. 4; S7A).

To further evaluate the potential interaction between detrital sediments and pore water/seawater Nd isotope composition, we can use the results from two detrital sediment samples from the siliceous chalk unit (section 33R-6) and from the nannofossil-bearing diatom ooze unit (section 26R-2) at Site 278. The detrital samples exhibit $\varepsilon_{Nd(t)}$ values of -10.4 ± 0.3 and -7.9 ± 0.3, respectively (Fig. 4; Table S5), within the range of terrigenous inputs from Paleozoic granites and metasedimentary rocks ($\varepsilon_{Nd(t)=}$ -4.9 to -13.9) of the South Island, New Zealand (Pickett and Wasserburg 1989). This observation is in line with the general deep water flow in the area, suggesting that terrigenous sediments in the Southern Emerald Basin are predominantly derived from the erosion of the New Zealand´s Southern Alps via the Solander Channel (Carter and McCave, 1997). Importantly, the measured detrital sediment composition is more unradiogenic (i.e. more negative ε_{Nd} values) than the almost contemporaneous fish debris signatures and hence cannot be responsible for the observed more radiogenic values. In addition, REE patterns from a fish debris sample from section 33R-6 (~30.5 Ma) exhibit a pattern enriched in middle-REEs and a prominent negative cerium (Ce) anomaly, which represent diagnostic features of uncontaminated seawater origin in the fish debris (Fig. 5; Table S6) (Scher et al., 2011; Huck et al., 2016, 2017). The fish debris sample from section 26R-2 (21.8 Ma) exhibit also a typical middle-REEs enriched pattern but records a slightly positive Ce anomaly (Fig. 5). Positive Ce anomalies in fish debris have been linked to anoxic seawater and/or pore water conditions, resulting in remobilization of REEs from authigenic or organic matter coatings (Elderfield and Pagett, 1986; Freslon et al., 2014; Huck et al., 2016). High

biogenic productivity at Site 278 associated with proto-polar front upwelling processes (Kennett et al., 1975) may have led to anoxic conditions at the seafloor.

Similar to Site 278, bulk sediment results from Site 274 exhibit a less radiogenic (i.e. lower) Nd isotope fingerprint than fish debris when comparing results for the same samples and samples taken very close to each other. The difference in $\varepsilon_{Nd(t)}$ for three pairs of fish debris-detrital sediment samples analyzed is -4.9, -3.5 and -2.4 ε_{Nd} units, while adjacent samples show differences in $\varepsilon_{Nd(t)}$ of -2.5 and -1.1 (Figs. 4; S7B; Table S5). This pronounced difference between the $\varepsilon_{Nd(t)}$ values of the fish debris and the detrital sediment samples at Site 274 strongly supports the absence of significant exchange between the detrital sediments and the fish debris. Overall, the more radiogenic $\varepsilon_{Nd(t)}$ values of the fish debris, compared to the more unradiogenic $\varepsilon_{Nd(t)}$ values of the detrital samples, argues against a contribution of Nd from the detrital sediments.

Furthermore, REE patterns of three fish debris samples at Site 274 yielded middle-REE bulge patterns, including a slightly positive Ce anomaly (Figs. 5; Table S6). The close proximity of Site 274 to the Antarctic continental margin and the high biogenic fraction in the sediment (Hayes et al., 1975) may have caused the observed positive Ce anomaly resulting from increased weathering inputs and/or remobilized REEs from authigenic or organic matter coatings due to anoxic conditions in the pore waters (Elderfield and Pagett, 1986; Freslon et al., 2014; Huck et al., 2016). Further work is required to fully understand the positive Ce anomaly in our fish debris samples. Nevertheless, REE patterns from Site 278 and 274 are similar to REE patterns from Eocene-Oligocene fish debris records from around the Tasmanian Gateway, which have been interpreted to preserve a predominantly seawater signature, despite positive Ce anomalies (Huck et al., 2016, 2017). We therefore suggest an authigenic nature of the fish debris record from Sites 278 and 274 and use our new data to explore the chemical

fingerprint of proto-CDW and RSBW across the Tasmanian Gateway, and its implications for the ACC evolution.

5.2 Early Oligocene epoch (33 -30 Ma): Prior to the inferred onset of the ACC throughflow via the Tasmanian Gateway

Neodymium isotope values from our deeper Site 278 (paleodepth: ~4000 m) between 31and 30 Ma, indicate that the southern Emerald Basin was bathed by an unradiogenic deep water mass ($\varepsilon_{Nd(t)}$ = ~-6.4) (Figs. 4; 6). These values converge with published Nd isotope records from the deep South Pacific (Site U1370, paleodepth ~5000 m, Site 596 paleodepth ~5000 m and Site 323, paleodepth ~4000 m; $\varepsilon_{Nd(t)}$ = ~-6.3) (Thomas et al. 2014; McKinley et al., 2019), suggesting that abyssal sites in the South Pacific were likely influenced by a common deep/bottom water mass, such as South Pacific Deep Water (SPDW) (Fig. 6). Temporal and spatial Nd isotope patterns and modelling results show that SPDW was a prominent and persistent water mass of the deep (≥ 3500 m) South Pacific (between at least ~30°S-63°S) from 70 to 20 Ma, characterised by $\varepsilon_{Nd(t)}$ of ~ -6 (Thomas et al. 2014; McKinley et al., 2019; Sarkar et al., 2019). We therefore suggest that Site 278 (paleolocation: ~63°S) was bathed by SPDW between 33 and 30 Ma.

Neodymium isotope records consistent with model results indicate bimodal mode of deep ocean circulation in the Pacific Ocean from ~70 to 25 Ma (Scher, 2014; Thomas et al., 2014; Scher et al., 2015; Huck et al., 2017; McKinley et al., 2019; Sarkar et al., 2019). Convection of SPDW occurred in the South Pacific (likely in the Ross Sea region), while North Pacific Deep Water (NPDW) formation occurred in the North Pacific. Our $\varepsilon_{Nd(t)}$ values from Site 274, located proximal to the Ross Sea, however, range from -3.1 to -5 between 33.5 and 29.7 Ma and albeit of low resolution are more radiogenic (less negative), compared to both the present-day RSBW Nd isotopic composition (ε_{Nd}= -6.4 to -7.5; Rickli et al., 2014; Basak et al.,

2015) and the deep record from Site 278 (Figs. 4; 6). The average $\varepsilon_{Nd(t)}$ value of ~ -4.6 for the early Oligocene (~ 33.5-29.7 Ma) at Site 274 (paleodepth: ~ 2500-3000 m) overlaps with published data from the East Tasman Plateau (Site 1172; average $\varepsilon_{Nd(t)}$ =~ -4.2 paleodepth: ~ 2400 m) and Hikurangi Plateau (Site 1124; average $\varepsilon_{Nd(t)}$ = ~-4.6; paleodepth: ~3000 m) (Scher et al., 2015; Sarkar et al., 2019) (Fig. 6). Similarities in Nd isotope values and paleodepths between the Antarctic margin record from Site 274 and the published records for the northern parts of the Tasmanian Gateway (Sites 1172 and 1124; Scher et al. 2015), suggest that these sites may have been influenced by a common water mass, occupying water depths between ~ 2500and 3000 m. This more radiogenic signature is akin to northern sources Equatorial Pacific Deep Water (Fig. 6) (Scher, 2014), which originated in the deep Equatorial Pacific, where NPDW and SPDW mixed (Thomas et al., 2014). Neodymium isotope data from Sites 1172 and 1124 suggest that Equatorial Pacific water was present at 2500-3000 m, reaching at least to southern latitudes of 60°S-65°S between 36 and 30 Ma (Scher et al., 2015; Sarkar et al., 2019). We here suggest that water from a northern source with a more Equatorial Pacific-like Nd isotope signature reached to the Adare Basin (Site 274, ~70°S) between 33 and 30 Ma.

Our results point to the presence of two distinct deep water masses in the late Eocene/early Oligocene South Pacific: one occupying depths between ~2500 and 3000 m with Nd composition ($\varepsilon_{Nd(t)=}$ ~-3 to -5) and a second deep/bottom water mass (> 3000 m) with more unradiogenic Nd composition ($\varepsilon_{Nd(t)=}$ ~-6) (Fig. 6).

FIGURE 6

5.3 Early Oligocene to early Miocene epoch (30-22 Ma): After the inferred onset of the ACC throughflow via the Tasmanian Gateway

Neodymium isotope values at Site 274 show a shift towards less radiogenic values ($\varepsilon_{Nd(t)}$ = -6.2 ± 0.3) between 29.7 and 29.1 Ma. Slightly less radiogenic $\varepsilon_{Nd(t)}$ values are observed around 24.3 Ma and 24.0 Ma (-7.3 ± 0.25 and -6.8 ± 0.15, respectively) (Figs. 4; 6), resembling modern RSBW values (ε_{Nd}= -6.4 to -7.5; Rickli et al., 2014; Basak et al., 2015). The shift between 29.7 and 29.1 Ma at Site 274 coincides with the shift observed in the two Nd isotope records from the East Tasman Plateau (Site 1172 $\varepsilon_{Nd(t)}$ = -4.8 to -6.8) and the Hikurangi Plateau (Site 1124 $\varepsilon_{Nd(t)}$ = -5.6 to -6.2) between 29.6 and 29 Ma, respectively (Scher et al., 2015) (Fig. 6). This latter shift has been linked to the northward migration and alignment of the Tasmanian Gateway with the westerly winds (Scher et al., 2015). The change in the $\varepsilon_{Nd(t)}$ values at Site 274 between 29.7 and 29.1 Ma does not coincide with any significant known change in the Antarctic ice sheet that would have influenced the sediment input around the Ross Sea. Instead, given that Site 274 was located south of the proto-PF during this period (Nelson and Cooke, 2001; Scher et al., 2015), we posit that the shift to more unradiogenic Nd contribution is probably due to the onset of proto-CDW upwelling reaching the Adare Basin and Site 274.

Site 278, on the other hand, was located close to the proto-PF and proto-SAF between 30 Ma and 22 Ma and thus in the main pathway of the proto-ACC and proto-CDW (Nelson and Cooke, 2001), explaining its invariant Nd isotope fingerprint (average $\varepsilon_{Nd(t)}$ = -6.4) throughout the early Oligocene to early Miocene (29.7-22 Ma) (Figs. 4; 6). These values are matched by the two published Nd isotope records (Sites 1172 and 1124; $\varepsilon_{Nd(t)}$ ~-6.5) from the eastern side of Tasmanian Gateway after the onset of ACC influence at this northern location (Scher et al., 2015) (Fig. 5). All three records show more radiogenic Nd isotope compositions than modern CDW in the Emerald Basin (ε_{Nd} = -9; Lambelet et al., 2018) (Figs. 2A; S2). They furthermore differ from records to the west of the Tasmanian Gateway. Throughout the Oligocene (30-23 Ma) Nd isotope records along the proto-PF in the South Atlantic and the South Indian Ocean are characterised by proto-CDW with a Nd isotope composition between

~ -7 and -9 (Site 689: Scher and Martin, 2004; Site 748 and 744: Wright et al., 2018; Site 269: Evangelinos et al., 2020) (Figs. 6; 7). Such values are similar to modern CDW (ε_{Nd}= -8.3 ± 1.5, n=158) (Lambelet et al., 2018) (Fig. 6).

Comparison between our new and previously published data along the proto-ACC pathway around the Tasmanian Gateway therefore reveals a provinciality in seawater Nd isotopes with more radiogenic proto-CDW ($\varepsilon_{Nd(t)}$ = -6 to -7.5) on the Pacific side of the Tasmanian Gateway, and less radiogenic proto-CDW ($\varepsilon_{Nd(t)}$= -7 to -9) in the Indian and Atlantic sectors of the Southern Ocean (Figs. 6; 7). This observation implies an absence of a homogenous deep water mass across the Tasmanian Gateway during the Oligocene and early Miocene, and suggests a more complex evolution of the deep ocean circulation across the gateway than previously assumed.

We propose that the provinciality in water mass signatures across the gateway was due to a less deep reaching and probably also weaker proto-ACC flow during the Oligocene to early Miocene (Fig. 7). A shallower and weaker ACC flow entering the South Pacific would have increased the amount of time that Pacific deep water could have mixed with the proto-CDW, allowing for acquisition of a more radiogenic isotopic composition of proto-CDW. These inferences are consistent with numerical simulations showing limited throughflow of the proto-ACC due to Australasian paleogeography during the Oligocene (Hill et al., 2013) and weaker global overturning circulation due to weaker westerly winds from the early to mid-Miocene (Herold et al, 2012).

Recently collected sedimentological data, microfossil assemblages and past reconstructions of sea surface temperatures from the Antarctic-Australian Basin and around the Tasmanian Gateway, also infer a weaker proto-ACC frontal system, characterised by intrusions of warm waters from northern latitudes from the Oligocene to the middle Miocene, weak latitudinal paleotemperature gradients and absence of strong sea ice seasonality (34-11

Ma) (Bijl et al., 2018; Hartman et al., 2018; Salabarnada et al., 2018; Sangiorgi et al., 2018; Evangelinos et al., 2020; Hoem et al., 2021). The question remains when the modern-like ACC was established. Our data suggest that this occurred during the Neogene, but future work is necessary to address the timing of its establishment and the wider implications of a weaker Oligocene to Miocene ACC.

FIGURE 7

5.4 Evidence of a glacial weathering event during the latest Oligocene (~25 Ma)

The most pronounced ε_{Nd} excursion observed at Site 274 (from -6.8 ± 0.3 to -3.7 ± 0.3) between 24.0 and 23.8 Ma is a peculiar feature of our new record and may reflect a local change in seawater composition (Figs. 4; 6). Although only represented by a single data point, another radiogenic isotope excursion is hinted at ~ 33.5 Ma ($\varepsilon_{Nd(t)}$ = -3.1 ± 0.3; Figs. 4; 6). Considering the relatively invariant Nd isotope compositions of Oligocene Pacific deep water (Scher, 2014; McKinley et al., 2019) and proto-CDW (this study; Wright et al., 2018; Evangelinos et al., 2020) during the Oligocene, we consider two potential causes for the radiogenic excursion at Site 274: (i) increased boundary exchange/volcanic activity, and (ii) pulses in Antarctic ice advance leading to increased weathering inputs to local seawater.

Volcanic activity and deposition of material from the McMurdo volcanic group (ε_{Nd} > 0; see references in Cook et al., 2013) have been reported to occur predominantly after 24 Ma (Roberts et al., 2013). In addition, there is little physical evidence of volcanic contributions to the sediments at Site 274 (Hayes et al., 1975), an observation that is confirmed by our measured detrital sediment $\varepsilon_{Nd(t)}$ values of -8.5 ± 0.3 (Fig. 4). Furthermore, REE patterns indicate that fish debris predominantly preserve a seawater signature at 23.8 Ma (Fig. 5). We therefore

499 exclude the possibility of boundary exchange/volcanic activity as a cause for the positive Nd
500 isotope excursion.

501 A more promising connection can be made with the timing of a major expansion of ice
502 from Antarctica. The Eocene-Oligocene transition is well documented as a major ice advance
503 on Antarctica (e.g., Zachos et al., 1992; Galeotti et al., 2016). A seawater expression of
504 weathering inputs from this ice expansion has been documented in the Prydz Bay area, where
505 late Eocene and Eocene Oligocene Transition (EOT) fish teeth show a shift in seawater
506 composition consistent with increased Antarctic weathering inputs (Scher et al., 2011; Bohaty
507 et al., 2012; Wright et al., 2018). Even though only documented by a single data point, the very
508 radiogenic $\varepsilon_{Nd(t)}$ value of -3.1 ± 0.3, our Site 274 exhibits the most extreme Nd isotope signature
509 ~ 33.5 Ma (Figs. 4; 6). A shift towards more radiogenic values may indicate erosion and
510 delivery of more radiogenic material exposed upstream in the Transantarctic Mountains, such
511 as basalts and sills of the Ferrar Large Igneous Province (ε_{Nd}: -3.5 to -6.9; see Cook et al., 2013
512 for a summary) or rocks like the Granite Harbour Intrusives in the Gabbro Hills (ε_{Nd} =~ -2.3 ±
513 1.6, n=4; Borg et al., 1990).

514 Interestingly, our data clearly define a second major seawater Nd isotope excursion
515 between 24.0 and 23.8 Ma, which appears to be closely associated with one of the most
516 significant climate transitions since the EOT resulting in a major Antarctic ice sheet expansion
517 (~24.5-24 Ma; Levy et al., 2019). Kulhanek et al. (2019) described the first occurrence of ice
518 proximal glaciomarine sediments from DSDP Site 270 on the shelf of the Ross Sea at this time.
519 In addition disconformities are observed at another Ross Sea drill site proximal to the
520 Transantarctic Mountains (CRP-2/2A; Naish et al., 2008), and in seismic data (Sorlien et al.,
521 2007), which are consistent with the first major expansion of marine ice sheets across the Ross
522 Sea continental shelf (see also Levy et al., 2019). We consider it very likely that large changes
523 in the Antarctic cryosphere, i.e. large ice advance in this case, would have changed significantly

524 the erosional input from Antarctica to the Ross Sea margin, and hence would have imprinted a
525 radiogenic Nd isotope signal in local seawater.
526
527 **6. CONCLUSIONS**

528 New Oligocene to Miocene seawater Nd isotope data from Site 274 in the Adare Basin, Ross
529 Sea, reveal two major shifts in seawater chemistry in response to major steps in Antarctic ice
530 sheet expansion at the Eocene/Oligocene boundary (33.7 Ma) and between ~24.5 and 24.0 Ma.
531 In contrast, Site 278 in the southern Emerald Basin shows an invariant Nd isotopic composition
532 ($\varepsilon_{Nd(t)}$ = -6.0 to -6.7) throughout the Oligocene and early Miocene (31-22 Ma). Comparison
533 with previously published data suggests the presence of two deep water masses in the South
534 Pacific prior to the inferred onset of the ACC (34-30 Ma), one occupying depths between
535 ~2500 and3000 m with Nd composition $\varepsilon_{Nd(t)=}$ -3 to -5 and a deep/bottom water mass (>3000
536 m) with more unradiogenic Nd composition ($\varepsilon_{Nd(t)=}$ ~-6). Following the onset of the ACC and
537 the opening of the Tasman Gateway (30-22 Ma), the seawater Nd isotope record at Site 278,
538 remained more radiogenic than the proto-CDW in the South Atlantic and Indian Ocean. We
539 attribute the provinciality in the Nd isotope composition of deep waters across the Tasmanian
540 Gateway to a weaker, less deep reaching ACC (proto-ACC) than today. Our finding implies
541 that the modern strong and deep-reaching ACC, which creates a near homogenous Southern
542 Ocean Nd isotope fingerprint must developed at a later point in the Neogene.
543
544 **Acknowledgments**
545
546 This research used samples provided by the International Ocean Discovery Program (IODP).
547 We acknowledge the staff and shipboard party from Legs 28 and 29. We thank the staff at the
548 Gulf Coast core repository (GCR) for curating these cores and assistance in core handling and

549 shipping. We also acknowledge the Paleomagnetic Laboratory of Barcelona (CSIC-CCiTUB).
550 We also thank Denise Kulhanek and an anonymous reviewer for their constructive comments,
551 which improved this paper. Funding to this research is provided by the Alexander S. Onassis
552 Public Benefit Foundation Ph.D. research grant: F ZL 016-1/2015-2016; the Spanish Ministry
553 of Economy, Industry and Competitivity (grants CTM2017-89711-C2-1/2-P), co-funded by
554 the European Union through FEDER funds; and an ECORD Research grant awarded to DE.
555 PKB and FH acknowledge funding through the European Research Council starting grant
556 #802835 OceaNice and NWO polar programme grant ALWPP2016.001. This paper is a
557 contribution to the SCAR PAIS Programme.

558

559 **Data availability**

560 The datasets to this article are available in the Supplement.

561

562 **Appendix A. Supplementary data:** Supplementary figures and tables

563

564 **REFERENCES**

565 Amakawa, H., Sasaki, K., and Ebihara, M., 2009. Nd isotopic composition in the central North
566 Pacific. Geochimica et Cosmochimica Acta, 73(16), 4705–4719.
567 https://doi.org/10.1016/j.gca.2009.05.058
568 Basak, C., Pahnke, K., Frank, M., Lamy, F., & Gersonde, R., 2015. Neodymium isotopic
569 characterization of Ross Sea Bottom Water and its advection through the southern South
570 Pacific. Earth and Planetary Science Letters, 419, 211–221.
571 https://doi.org/10.1016/j.epsl.2015.03.011.
572 Bijl, P. K., Bendle, A. P. J., Bohaty, S. M., Pross, J., Schouten, S., Tauxe, L., Stickley, C. E., McKay,
573 R. M., Röhl, U., Olney, M., Sluijs, A., Escutia, C., Brinkhuis, H., and Expedition 318 scientists,
574 2013. Eocene cooling linked to early flow across the Tasmanian Gateway, P. Natl. Acad. Sci.
575 USA, 110, 9645–9650.
576 Bijl, P. K., Houben, A. J. P., Hartman, J. D., Pross, J., Salabarnada, A., Escutia, C., and Sangiorgi, F.,
577 2018. Paleoceanography and ice sheet variability offshore Wilkes Land, Antarctica – Part 2:

578 Insights from Oligocene–Miocene dinoflagellate cyst assemblages, Clim. Past, 14, 1015–1033,
579 https://doi.org/10.5194/cp-14-1015-2018.
580 Biscaye, P.E., 1965. Mineralogy and sedimentation of recent deep-sea clay in the Atlantic Ocean and
581 adjacent seas and oceans. Geol. Soc. Am. Bull.76 (7), 803–832.
582 Bohaty S.M., Zachos, J.C., Delaney, M.L., 2012. Foraminiferal Mg/Ca evidence for Southern Ocean
583 cooling across the Eocene-Oligocene transition, Earth and Planetary Science Letters 317-318
584 (2012), 251-261.
585 Borg, S. G., Depaolo, D. J., and Smith, B. M., 1990. Isotopic structure and tectonics of the central
586 Transantarctic Mountains. Journal of Geophysical Research: Solid Earth, 95(B5), 6647-6667.
587 Carter, L., McCave, I.N., 1997. The sedimentary regime beneath the Deep Western Boundary Current
588 infow to the Southwest Pacific Ocean. J. Sediment. Res. 67, 1005-1017.
589 Cook, C.P., van de Flierdt, T., Williams, T., Hemming, S.R., Iwai, M., Kobayashi, M., Jimenez-
590 Espejo, F.J., Escutia, C., Gonzalez, J.J., Khim, B.-K., McKay, R.M., Passchier, S., Bohaty,
591 S.M., Riesselman, C.R., Tauxe, L., Sugisaki, S., Galindo, A.L., Patterson, M.O., Sangiorgi,
592 F., Pierce, E.L., Brinkhuis, H., Klaus, A., Fehr, A., Bendle, J.A.P., Bijl, P.K., Carr, S.A.,
593 Dunbar, R.B., Flores, J.A., Hayden, T.G., Katsuki, K., Kong, G.S., Nakai, M., Olney, M.P.,
594 Pekar, S.F., Pross, J., Rohl, U., Sakai, T., Shrivastava, P.K., Stickley, C.E., Tuo, S., Welsh,
595 K., Yamane, M., 2013. Dynamic behaviour of the East Antarctic ice sheet during Pliocene
596 warmth. Nat. Geosci.6 (9), 765–769. https://doi .org /10 .1038 /ngeo1889.
597 Chavagnac, V., Milton, J., Green, D., Breuer, J., Bruguier, O., Jacob, D., Jong, T., Kamenov, G., Le
598 Huray, J., and Liu, Y., 2007. Towards the development of a fossil bone geochemical standard:
599 An inter-laboratory study, *Analytica Chimica Acta*, *599*(2), 177-190.
600 Conway, C. E., Bostock, H. C., Baker, J. A., Wysoczanski, R. J., & Verdier, A., 2012. Evolution of
601 Macquarie Ridge Complex seamounts: Implications for volcanic and tectonic processes at the
602 Australia-Pacific plate boundary south of New Zealand. Marine Geology, 295-298, 34–50.
603 https://doi.org/10.1016/j.margeo.2011.11.009
604 Dalziel, I. W. D., 2014. Drake Passage and the Scotia arc: A tortuous space-time gateway for the
605 Antarctic Circumpolar Current. Geology (2014) 42 (4):367-368.
606 https://doi.org/10.1130/focus042014.1
607 Dijkstra, A. H., Sergeev, D. S., Spandler, C. A., Pettke, T., Meisel, T., and Cawood, P. A., 2009.
608 Highly refractory peridotites on Macquarie Island and the case for anciently depleted domains
609 in the Earth' s mantle. Journal of Petrology, 51(1-2), 469–493.
610 https://doi.org/10.1093/petrology/ egp084
611 Elderfield, H., and Pagett, R., 1986. Rare earth elements in ichthyoliths: variations with redox
612 conditions and depositional environment, *Science of the Total Environment*, *49*, 175-197.
613 Evangelinos D., Escutia, C., Etourneau, J., Hoem, F., Bijl, P., Boterblom, W., van de Flierdt, T.,
614 Valero, L., Flores, J. A., Rodriguez-Tovar, F., Jimenez-Espejo, F., Salabarnada, A., López-

615 Quirós, A., 2020. Global and Planetary Change 191, 103221.
616 https://doi.org/10.1016/j.gloplacha.2020.103221.
617 Freslon, N., Bayon, G., Toucanne, S.. Bermell, S., Bollinger, C., Chéron, S., Etoubleau, J., Germain,
618 Y., Khripounoff, A., Ponzevera, E., 2014. Rare earth elements and neodymium isotopes in
619 sedimentary organic matter, Geochimica Et Cosmochimica Acta, 140, 177-198.
620 https://doi.org/10.1016/j.gca.2014.05.016.
621 Galeotti, S., DeConto, E., Naish, T., Stocchi, P., Florindo, F., Pagani, M., Barrett, P., Bohaty, S.M.,
622 Lanci, L., Pollard, D., Sandroni, S., Malarico, F.M., Zachos, J.C., 2016. Antarctic Ice Sheet
623 variability across the Eocene-Oligocene boundary climate transition. Science, 352(6281), 76-
624 80. https://doi.org/10.1126/science.aab0669.
625 Garcia-Solsona, E., Jeandel, C., Labatut, M., Lacan, F., Vance, D., Chavagnac, V., & Pradoux, C.,
626 2014. Rare earth elements and Nd isotopes tracing water mass mixing and particle-seawater
627 interactions in the SE Atlantic. Geochimica et Cosmochimica Acta, 125, 351–372. https://
628 doi.org/10.1016/j.gca.2013.10.009
629 Gordon, A.L., Orsi, A.H., Muench, R., Huber, B.A., Zambianchi, E., Visbeck, M., 2009. Western Ross
630 Sea continental slope gravity currents. Deep-Sea Research II 56 796-817.
631 Gradstein, F. M., Ogg, J. G., Schmitz, M. D., and Ogg, G. M., 2012. The Geologic Time Scale 2012,
632 The Geologic Time Scale 2012 2, 437–1144.
633 Hartman, J. D., Sangiorgi, F., Salabarnada, A., Peterse, F., Houben, A. J. P., Schouten, S., Escutia, C.,
634 and Bijl, P. K., 2018. "Paleoceanography and Ice Sheet Variability Offshore Wilkes Land ,
635 Antarctica – Part 3 : Insights from Oligocene – Miocene TEX 86 -Based Sea Surface
636 Temperature Reconstructions," 1275–97.
637 Hayes, D. E., and Frakes, L. A., 1975. General Synthesis, Deep Sea Drilling Project Leg 28, in Initial
638 Reports of the Deep Sea Drilling Project', US, 28, pp.19–48.
639 Herold, N., Huber, M., Müller, R.D., and M Seton, M., 2012. "Modeling the Miocene Climatic
640 Optimum: Ocean Circulation" 27 (December 2011): 1–22.
641 https://doi.org/10.1029/2010PA002041.
642 Hill, D. J., Haywood, A. M., Valdes, P. J., Francis, J. E., Lunt, D. J., Wade, B. S., and Bowman, V. C.,
643 2013. Paleogeographic controls on the onset of the Antarctic circumpolar current, Geophys.
644 Res. Lett., 40, 5199–5204, https://doi.org/10.1002/grl.50941.
645 Hoem, F. S., Valero, L., Evangelinos, D., Escutia, C., Duncan, B., McKay, R. M., Brinkhuis, H.,
646 Sangiorgi, F., Bijl, P., 2021. Temperate Oligocene surface ocean conditions offshore Cape
647 Adare, Ross Sea, Antarctica. Climate of the past 17, 1423-1442. https://doi.org/10.5194/cp-17-
648 1423-2021.
649 Huber, M., Brinkhuis, H., Stickley, C.E., Döös, K., Sluijs, A., Warnaar, J., Schellenberg, S.A.,
650 Williams, G.L., 2004. Eocene circulation of the Southern Ocean: was Antarctica kept warm
651 by subtropical waters? Paleoceanography 19. https:// doi .org /10 .1029 /2004PA001014.

Huck, C. E., van de Flierdt, T., Bohaty, S. M., and Hammond, S. J., 2017. Antarctic climate, Southern Ocean circulation patterns, and deep water formation during the Eocene, Paleoceanography, 32, 674–691, doi: 10.1002/2017PA003135

Huck, C. E., van de Flierdt, T., Jiménez‐Espejo, F. J., Bohaty S. M., Röhl, U., and Hammond, S. J, 2016. Robustness of fossil fish teeth for seawater neodymium isotope reconstructions under variable redox conditions in an ancient shallow marine setting, *Geochemistry, Geophysics, Geosystems*.

Jacobsen, S. B., & Wasserburg, G. J.,1980. Sm-Nd evolution of chondrites. Earth and Planetary Science Letters, 50, 139–155. https://doi.org/ 10.1016/0012-821X(80)90125-9

Kennett, J. P., Houtz, R. E., Andrews, P. B., Edwards, A. R., Gostin, V. A., Hajos, M., Hampton, M., Jenkins, D. G., Margolis, S. V., Ovenshine, A. T., Perch-Nielsen, K., 1975: Cenozoic paleoceanography in the southwest Pacific Ocean, Antarctic glaciation, and the development of the Circum- Antarctic Current. Initial Reports of the Deep Sea Drilling Project 29: 1155–1169.

Kulhanek, D. K., Levy, R. H., Clowes, C. D., Prebble, J. G., Rodelli, D., Jovane, L., Morgans, H. E., Kraus, C., Zwingmann, H., and Griffith, E. M, 2019. Revised chronostratigraphy of DSDP Site 270 and late Oligocene to early Miocene paleoecology of the Ross Sea sector of Antarctica, Global and Planetary Change, 178, 46-64. https://doi.org/10.1016/j.gloplacha.2019.04.002

Lambelet, M., van de Flierdt, T., Butler, E. C. V., Bowie, A. R., Rintoul, S. R., Watson, R. J., Remenyi, T., Lannuzel, D., Warner, M., Robinson, L.F., Bostock, H.C. and Bradtmiller, L.I, 2018. The neodymium isotope fingerprint of Adélie Coast Bottom Water. Geophysical Research Letters, 45, 11,247–11,256. https://doi.org/10.1029/2018GL080074

Lambelet, M., van de Flierdt, T., Crocket, K., Rehkämper, M., Kreissig, K., Coles, B., et al., 2016. Neodymium isotopic composition and concentration in the western North Atlantic Ocean: Results from the GEOTRACES GA02 section. Geochimica et Cosmochimica Acta, 177, 1–29. https://doi.org/10.1016/j.gca.2015.12.019

Levy, R.H., Meyers, S.R., Naish, T.R., Golledge, N.R., McKay, R.M., Crampton, J.S., DeConto, R.M., De Santis, L., Florindo, F., Gasson, E.G.W., Harwood, D.M., Luyendyk, B.P., Powell, R.D., Clowes, C., Kulhanek, D.K., 2019. Antarctic ice-sheet sensitivity to obliquity forcing enhanced through ocean connections. Nat. Geosci. 12, 132–137.

Martin, E. E., Haley B. A., 2000. Fossil fish teeth as proxies for seawater Sr and Nd isotopes. Geochim. Cosmochim. Acta 64, 835–847. (doi:10.1016/S0016-7037(99)00376-2)

McKinley, C. C., Thomas, D. J., LeVay, L., Rolewicz, Z. 2019. Nd isotopic structure of the Pacific Ocean 40-10 Ma, and evidence for the reorganization of deep North Pacific Ocean circulation between 36 and 25 Ma. Earth and Planetary Science Letters 521 (2019) 139-149.

688 Müller, R. D., Cannon, J., Qin, X., Watson, R. J., Gurnis, M., Williams, S., et al. 2018. GPlates:
689 Building a virtual Earth through deep time. Geochemistry, Geophysics, Geosystems, 19.
690 doi:10.1029/2018GC007584
691 Müller, R. D., Seton, M., Zahirovic, S., Williams, S. E., Matthews, K. J., Wright, N. M., Shephard, G.
692 E., Maloney, K., Barnett-Moore, N. and Hosseinpour, M. 2016. Ocean Basin Evolution and
693 Global-Scale Plate Reorganization Events Since Pangea Breakup, Annual Review of Earth and
694 Planetary Sciences, 44(1).
695 Naish, T.R., Wilson, G.S., Dunbar, G.B., Barrett, P.J., 2008. Constraining the amplitude of late
696 Oligocene bathymetric changes in western Ross Sea during orbitally-induced oscillations in the
697 East Antarctic Ice Sheet: (2) implications or global sea-level changes. Palaeogeogr.
698 Palaeoclimatol. Palaeoecol. 260, 66–76. https://doi.org/10. 1016/j.palaeo.2007.08.021.
699 Nelson, C. S., and Cooke, P.J., 2001. History of Oceanic Front Development in the New Zealand Sector
700 of the Southern Ocean during the Cenozoic—a Synthesis. *New Zealand Journal of Geology*
701 *and Geophysics* 44 (4): 535–53. https://doi.org/10.1080/00288306.2001.9514954.
702 Orsi, A. H., Whitworth, T., and Nowlin, W. D., 1995. On the meridional extent and fronts of the
703 Antarctic Circumpolar Current, Deep-Sea Res. Pt. I, 42, 641–673,
704 https://doi.org/10.1016/0967-0637(95)00021-W.
705 Pickett, D.A, Wasserburg, G. J., 1989. Neodymium and strontium isotopic characteristics of New
706 Zealand granitoids and related rocks. Contrib. Mineral Petrol 103, 131-142
707 Rickli, J., Gutjahr, M., Vance, D., Fischer-Gödde, M., Hillenbrand, C.-D., & Kuhn, G., 2014.
708 Neodymium and hafnium boundary contributions to seawater along the West Antarctic
709 continental margin. Earth and Planetary Science Letters, 394, 99–110
710 https://doi.org/10.1016/j.Bepsl.2014.03.008
711 Rintoul, S. R., 2018. The global influence of localized dynamics in the Southern Ocean. Nature 558
712 (7709): 209-218. https://doi.org/10.1038/s41586-018-0182-3.
713 Rintoul, S. R., 1998. On the origin and influence of Adélie Land Bottom Water. In Ocean, ice, and
714 atmosphere: Interactions at the Antarctic continental margin (Vol. 75, pp. 151–171).
715 Washington, DC: American Geophysical Union.
716 Rintoul, S. R., Sokolov, S., Williams, M. J. M., Peña Molino, B., Rosenberg, M., & Bindoff, N. L.,
717 2014. Antarctic Circumpolar Current transport and barotropic transition at Macquarie Ridge.
718 Geophysical Research Letters, 41, 7254–7261. https://doi.org/10.1002/2014GL061880.
719 Roberts, A. P., Sagnotti, L., Florindo, F., Bohaty, S. M., Verosub, K. L., Wilson, G. S., and Zachos, J.
720 C., 2013. Environmental record of paleoclimate, unroofing of the Transantarctic Mountains,
721 and volcanism in later Eocene to early Miocene glaci-marine sediments from the Victoria
722 Land Basin, Ross Sea, Antarctica, *Journal of Geophysical Research: Solid Earth, 118,* 1845-
723 186 1

Salabarnada, A., Escutia, C., Röhl, U., Nelson, C. H., McKay, R., Jiménez-Espejo, F. J., Bijl, P. K., Hartman, J. D., Strother, S. L., Salzmann, U., Evangelinos, D., López-Quirós, A., Flores, J. A., Sangiorgi, F., Ikehara, M., and Brinkhuis, H., 2018. Paleoceanography and ice sheet variability offshore Wilkes Land, Antarctica – Part 1: Insights from late Oligocene astronomically paced contourite sedimentation, Clim. Past, 14, 991–1014, https://doi.org/10.5194/cp-14-991-2018.

Sangiorgi, F., Bijl, P. K., Passchier, S., Salzmann, U., Schouten, S., McKay, R., Cody, R. D., Pross, J., Van De Flierdt, T., Bohaty, S. M., Levy, R., Williams, T., Escutia, C., Brinkhuis, H., 2018. Southern Ocean warming and Wilkes Land ice sheet retreat during the mid-Miocene. Nature Communications. 9, 317, doi:10.1038/s41467-017-02609-7

Sarkar, S., Basak, C., Martin, F., Berndt, C., Huuse, M., Badhani, S and Bailas, J., 2019. Late Eocene onset of the Proto-Antarctic Circumpolar Current. Scientific Reports, 9: 10125. https://doi.org/10.1038/s41598-019-46253-1.

Scher, H. D., 2014. Stacking PEAT; A stacked Nd isotope record for the Paleogene equatorial Pacific. Società Geologica Italiana, 31, 191-192 (doi: 10.3301/ROL.2014.115).

Scher H.D., Bohaty S.M., Zachos J.C. et al., 2011 – Two stepping into the icehouse: East Antarctic weathering during progressive ice-sheet expansion at the Eocene- Oligocene Transition. Geology, 39, 383-386.

Scher, H. D., and Martin, E. E., 2004. Circulation in the Southern Ocean during the Paleogene inferred from neodymium isotopes. Earth Planet. Sci. Lett. 228, 391–405.

Scher, H. D., Whittaker, J., William, S., Latimer, J., Kordesch, W., Delaney, M., 2015. Onset of Antarctic circumpolar current 30 million years ago as Tasmanian Gateway aligned with westerlies. Nature 523, 580–583.

Schlitzer, R, 2016. Ocean data view. Retrieved from odv.awi.de. https://doi.org/10.1182/blood-2012-03-418400

Scotese, C.R., & Wright, N., 2018. PALEOMAP Paleodigital Elevation Models (PaleoDEMS) for the Phanerozoic PALEOMAP Project, https://www.earthbyte.org/paleodem-resource-scotese-and-wright-2018.

Sijp, W.P., England, M.H., Huber, M., 2011. Effect of the deepening of the Tasman Gateway on the global ocean. Paleoceanography 26, 4207

Sokolov, S., & Rintoul, S. R., 2007. Multiple jets of the Antarctic Circumpolar Current south of Australia. Journal of Physical Oceanography, 37(5), 1394–1412. https://doi.org/10.1175/JPO3111.1

Sorlien, C.C., Luyendyk, B.P., Wilson, D.S., Bartek, L.R., Diebold, J.B., 2007. Oligocene development of the West Antarctic Ice Sheet recorded in eastern Ross Sea strata. Geology 35, 467–470.

Stichel, T., Frank, M., Rickli, J., & Haley, B. A, 2012. The hafnium and neodymium isotope composition of seawater in the Atlantic sector of the Southern Ocean. Earth and Planetary Science Letters, 317-318, 282–294. https://doi.org/10.1016/j.epsl.2011.11.025

Stichel, T., Pahnke, K., Duggan, B., Goldstein, S. L., Hartman, A. E., Paffrath, R., & Scher, H. D., 2018. *TAG Plume: Revisiting the Hydrothermal Neodymium Contribution to Seawater. Frontiers in Marine Science, 5.* doi:10.3389/fmars.2018.00096

Stickley, C.E., Brinkhuis, H., Schellenberg, S., Sluijs, A., Roehl, U., Fuller, M., Grauert, M., Huber, M., Warnaar, J., Williams, G.L., 2004. Timing and nature of the deepening of the Tasmanian Gateway. Paleoceanography 19, PA4027.

Tachikawa, K., V. Athias, and C. Jeandel, 2003. Neodymium budget in the modern ocean and paleo-oceanographic implications, Journal of Geophysical Research: Oceans (1978–2012), 108(C8).

Tanaka, T., Togashi, S., Kamioka, H., Amakawa, H., Kagami, H., Hamamoto, T., Yuhara, M., Orihashi, Y., Yoneda, S., Shimizu, H., Kunimaru, T., Takahashi, K., Yanagi, T., Nakano, T., Fujimaki, H., Shinjo, R., Asahara, Y., Tanimizu, M. & Dragusanu, C., 2000. JNdi-1: a neodymium isotopic reference in consistency with LaJolla neodymium. Chemical Geology, 168, 279-281.

Taylor, S. R., and McLennan, S. M., 1985. The continental crust: Its composition and evolution, 312 pp., Blackwell Scientific Publications, Oxford, U. K.

Thomas, D.J., Korty, R., Huber, M., Schubert, J.A., Haines, B., 2014. Nd isotopic structure of the Pacific Ocean 70–30 Ma and numerical evidence for vigorous ocean circulation and ocean heat transport in a greenhouse world. Paleoceanography 29, 454–469.

van de Flierdt, T., Griffiths, A. M., Lambelet, M., Little, S. H., Stichel, T., Wilson, D., 2016. Neodymium in the oceans: a global database, a regional comparison and implications for palaeoceanographic research. Philos. Trans. R. Soc. A 374, 20150293.

Weis, D., Kieffer, B., Maerschalk, C., Barling J., de Jong, J., Williams, G. A., Hanano, D., Pretorius, W., Mattielli, N., Scoates, J. S., 2006. High-precision isotopic characterization of USGS reference materials by TIMS and MC-ICP-MS, Geochemistry, Geophysics, Geosystems, 7(8), Q08006.

Wright, N., Scher, H. D., Seton, M., Huck, C. E., Duggan, B. D., 2018.No Change in Southern Ocean Circulation in the Indian Ocean From the Eocene Through Late Oligocene', Paleoceanography and Paleoclimatology, 33(2), pp. 152–167. doi: 10.1002/2017PA003238.

Zachos, J. C., Breza, J,. Wise, S. W., 1992. Earliest Oligocene ice-sheet expansion on East Antarctica: Stable isotope and sedimentological data from Kerguelen Plateau. Geology 20:569-573.

List of Figures

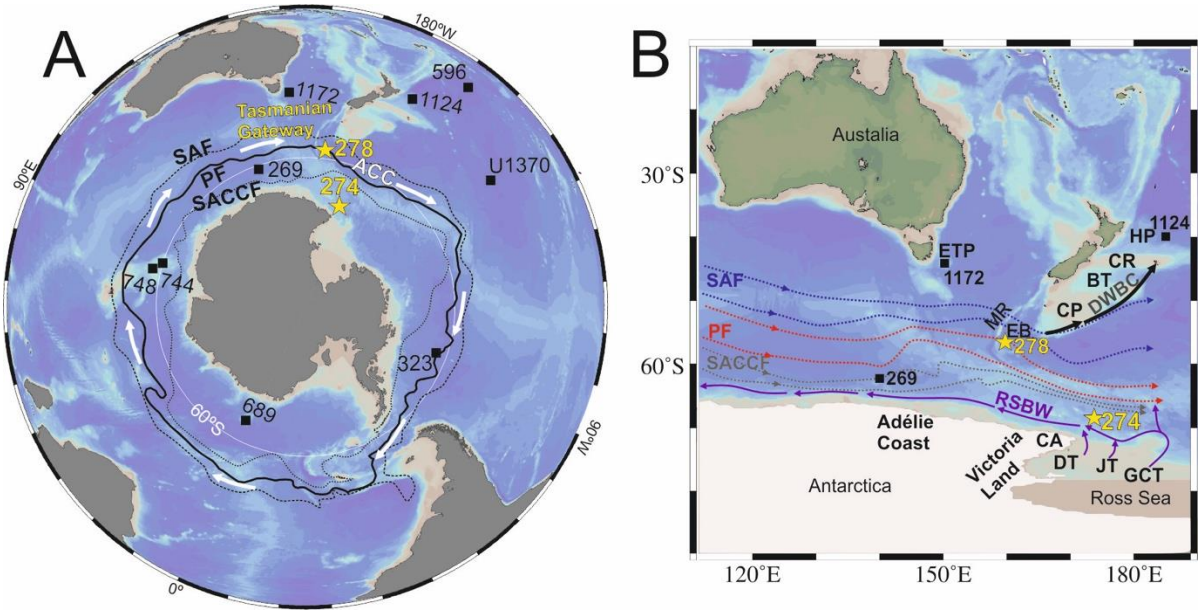

Figure 1. Overview map of modern Southern Ocean configuration (Ocean Data View, (Schlitzer, 2016; version 4.79; http://odv.awi.de). **A:** Antarctic Circumpolar Current (ACC) frontal system, study sites (DSDP Sites 274 and 278) (yellow stars) and sites referred to in this study (black squares). SAF: Subantarctic front (black dashed line), PF: Polar front (black line), SACCF: Southern Antarctic Circumpolar Current front (black dotted line) adapted from Orsi et al. (1995). **B:** Major modern deep ocean water circulation paths across the Tasmanian Gateway adapted from Sokolov and Rintoul. (2007) and Gordon et al. (2009). The main transport of Circumpolar Deep Water along the ACC takes place around the PF and SAF, Ross Sea bottom water (RSBW) (purple) feeds Antarctic Bottom Water. Deep Western Boundary Current (DWBC) (black arrows), MR: Macquarie Ridge, EB: Emerald Basin, ETP: East Tasman Plateau, CP: Campbell Plateau, BT: Bounty Trough, CR: Chatham Rise, HP: Hikurangi Plateau, CA: Cape Adare, JB: Joides Trough, DB: Drygalski Trough, GCT: Glomar Challenger Trough.

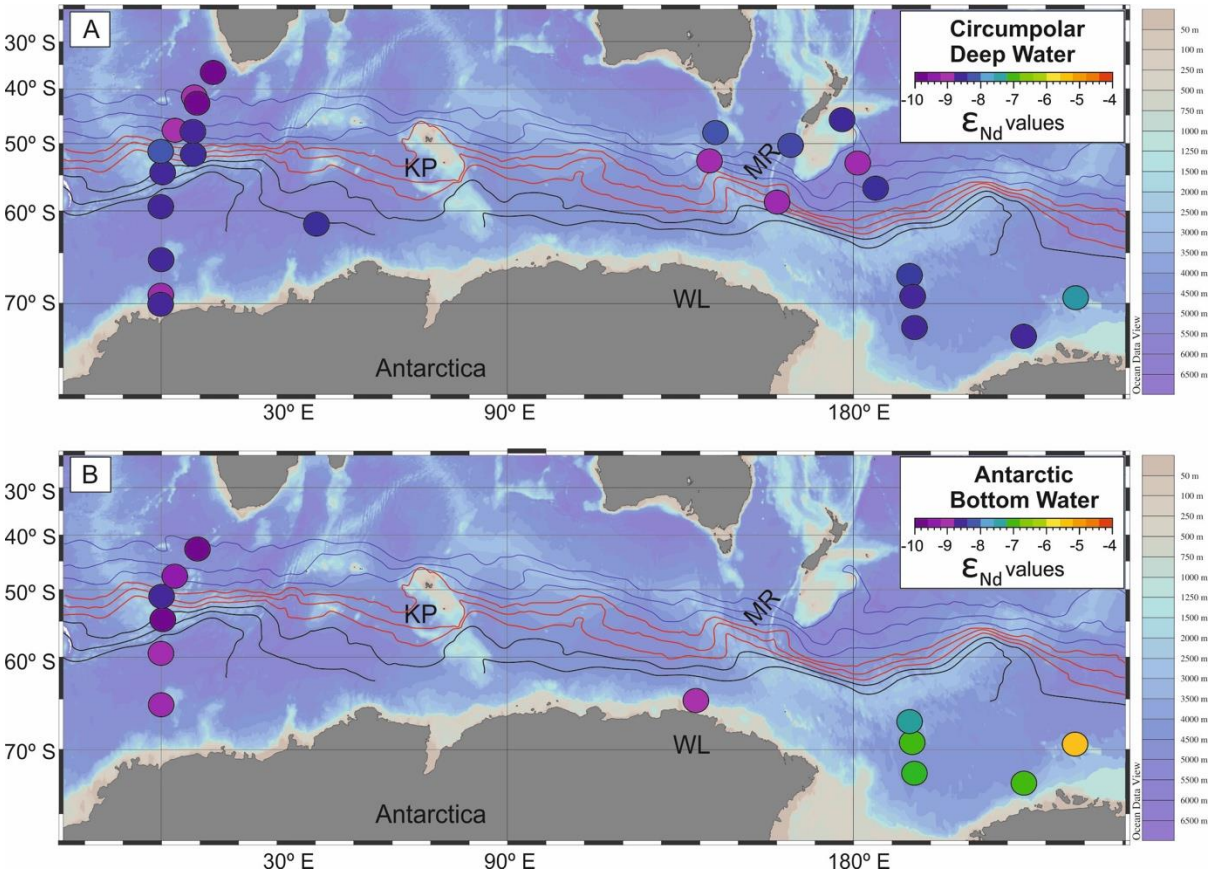

Figure 2. Modern neodymium (Nd) isotope composition for deep and bottom waters in the Southern Ocean (between 0°E and 110°W). Figures are made with Ocean Data View (Schlitzer, 2016; version 4.79; http://odv.awi.de). **(A):** Nd isotope composition of Circumpolar Deep Water (CDW). **(B):** Nd isotope composition of Antarctic Bottom Water (AABW) (Stichel et al., 2012; Rickli et al., 2014; Garcia-Solsona et al., 2014; Basak et al., 2015; Lambelet et al., 2018; Amakawa et al., 2019). Antarctic Circumpolar Current (ACC) fronts (mean positions) adapted from Sokolov and Rintoul, 2007. SAF (blue), PF (red), SACCF (black), MR: Macquarie Ridge, WL: Wilkes Land, KP: Kerguelen Plateau

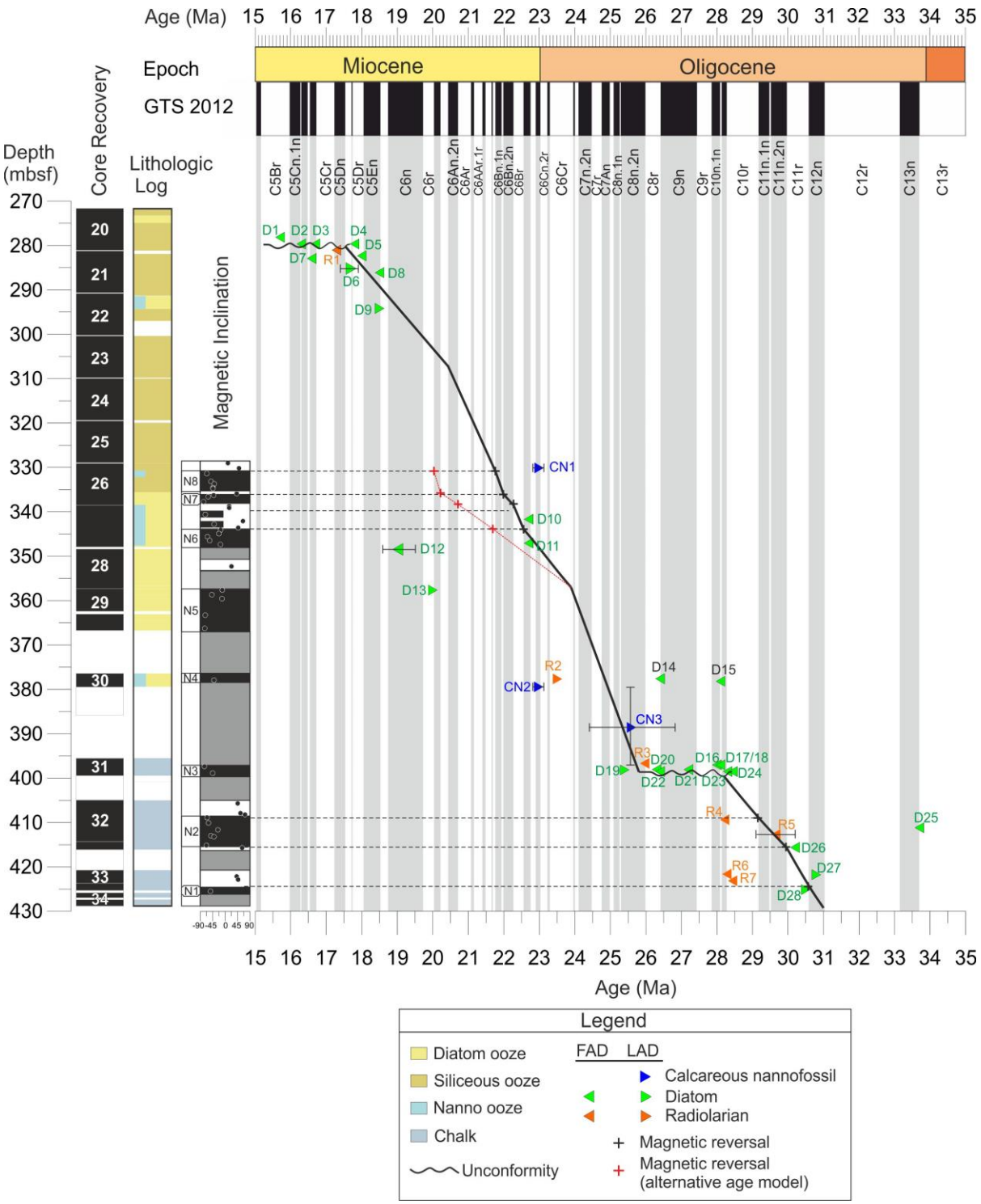

819

820 **Figure 3.** Revised age-depth model for Site 278. Stratigraphy of Site 278, from left to right:
821 depth in meters below sea floor (mbsf), core recovery, lithologic log based on initial shipboard
822 sedimentological descriptions and local polarity based on inclination values. Grey vertical
823 stripes mark the normal polarity zones of the geomagnetic polarity timescale (normal=black,
824 reversed=white) (Gradstein et al., 2012). Black/red crosses= magnetostratigraphic constraints,

green triangles= diatom biostratigraphic constraints, blue triangles = calcareous nannofossil biostratigraphic ranges, orange triangles= radiolarian biostratigraphic constraints. FAD=first appearance datum; LAD= last appearance datum . Horizontal error bars on biostratigraphic events indicate total age range for the given datum. Vertical error bars indicate the depth range for the given datum. Datum and biozone labels correspond to those in Tables: S1, S2, S3 and S4. The back line following the different constraints shows our preferred chronology, and in red a possible alternate.

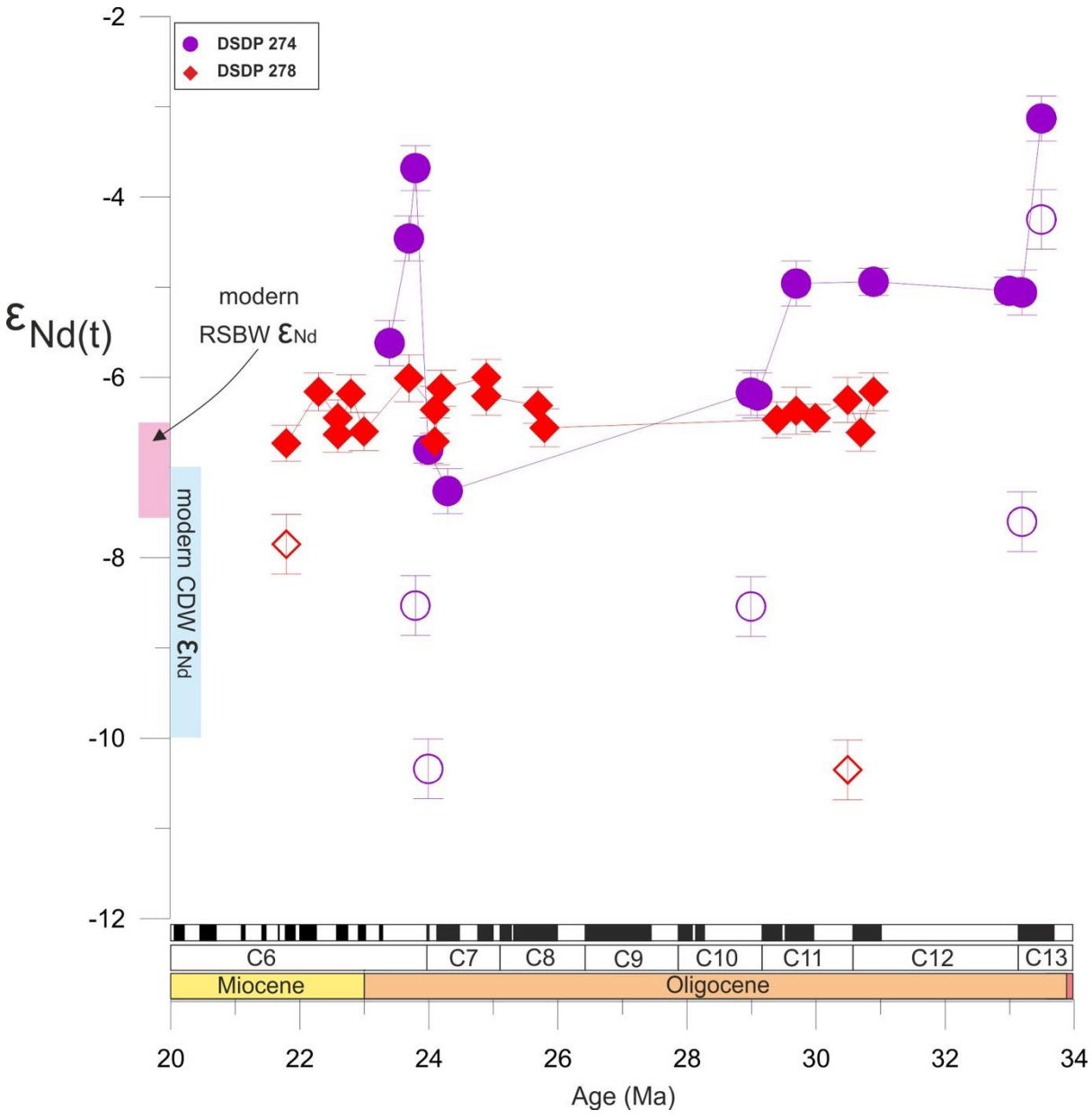

Figure 4. Fish debris $\varepsilon_{Nd(t)}$ records generated in this study from DSDP Sites 274 (purple circles) and 278 (red diamonds). Detrital sediment $\varepsilon_{Nd(t)}$ values from DSDP Sites 274 (purple open circles) and 278 (red open diamonds). Present-day Ross Sea Bottom Water (RSBW) ε_{Nd} endmember ranges shown in magenta (Rickli et al., 2014; Basak et al., 2015). Present-day Circumpolar Deep Water (CDW) ε_{Nd} endmember ranges shown in blue (Lambelet et al., 2018 and references therein).

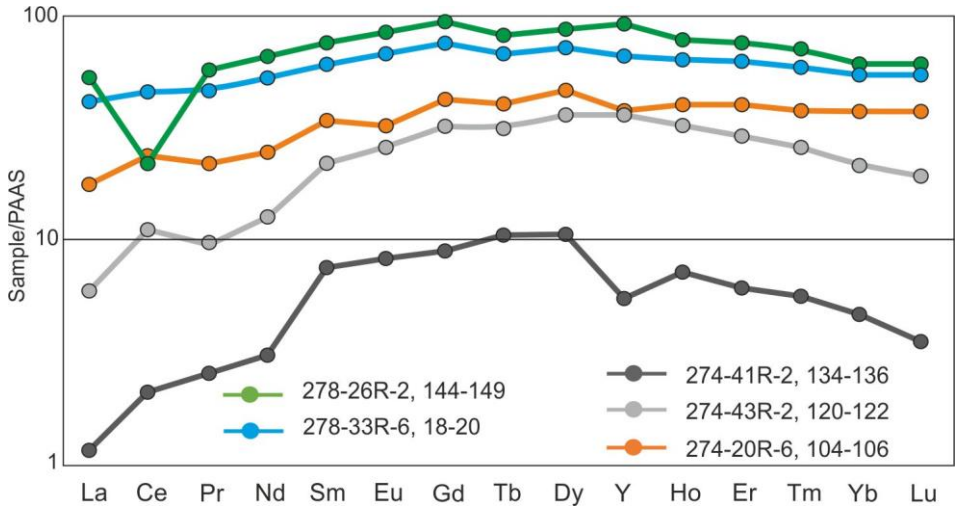

Figure 5. Rare earth element (REE) patterns normalised to Post Archean Shale (PAAS) concentrations (Taylor and McLennon, 1985) for DSDP Sites 278 and 274.

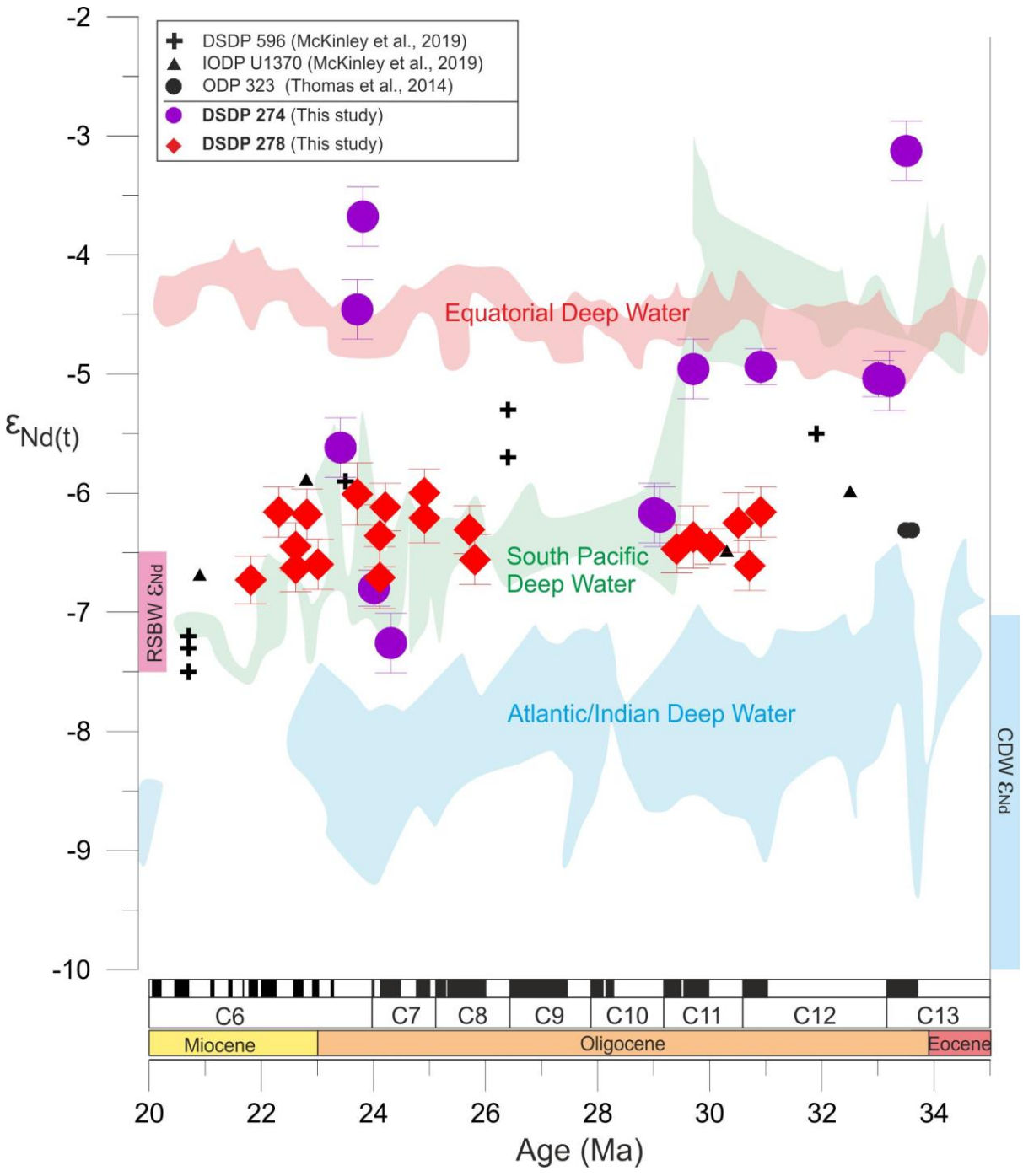

Figure 6. Comparison of fish debris ε_{Nd} records generated in this study from DSDP Sites 274 and 278 with those derived from sites along the proto-CDW path in the Atlantic, Indian and Pacific sectors of the Southern Ocean. Atlantic/Indian Ocean locations include ODP Site 689 (Maud Rise; Scher and Martin, 2004), ODP Sites 748 and 744 (Kerguelen Plateau; Wright et al., 2018), and DSDP Site 269 (off Adélie Coast; Evangelinos et al., 2020) (light blue shading). ODP Site 1124 (Hikurangi Plateau) and ODP Site 1172 (East Tasmanian Plateau; Scher et al.,

2015) are combined in the green shading. Pacific Equatorial Age Transect (PEAT) Nd isotope results from the Equatorial Pacific are based on IODP Sites U1331, U1332, U1333, U1334, and U1335 (Scher, 2014) (red shading). The only data shown as individual symbols other than our new results are South Pacific DSDP Site 596, IODP Site U1370 (McKinley et al., 2019) and ODP Site 323 (Thomas et al., 2014). Blue shaded ranges refer to the present-day Nd signature of the CDW and magenta shaded rangers refer to the present-day Nd isotopic composition of the RSBW (Rickli et al.,2014; Basak et al., 2015; Lambelet et al., 2018 and references therein).

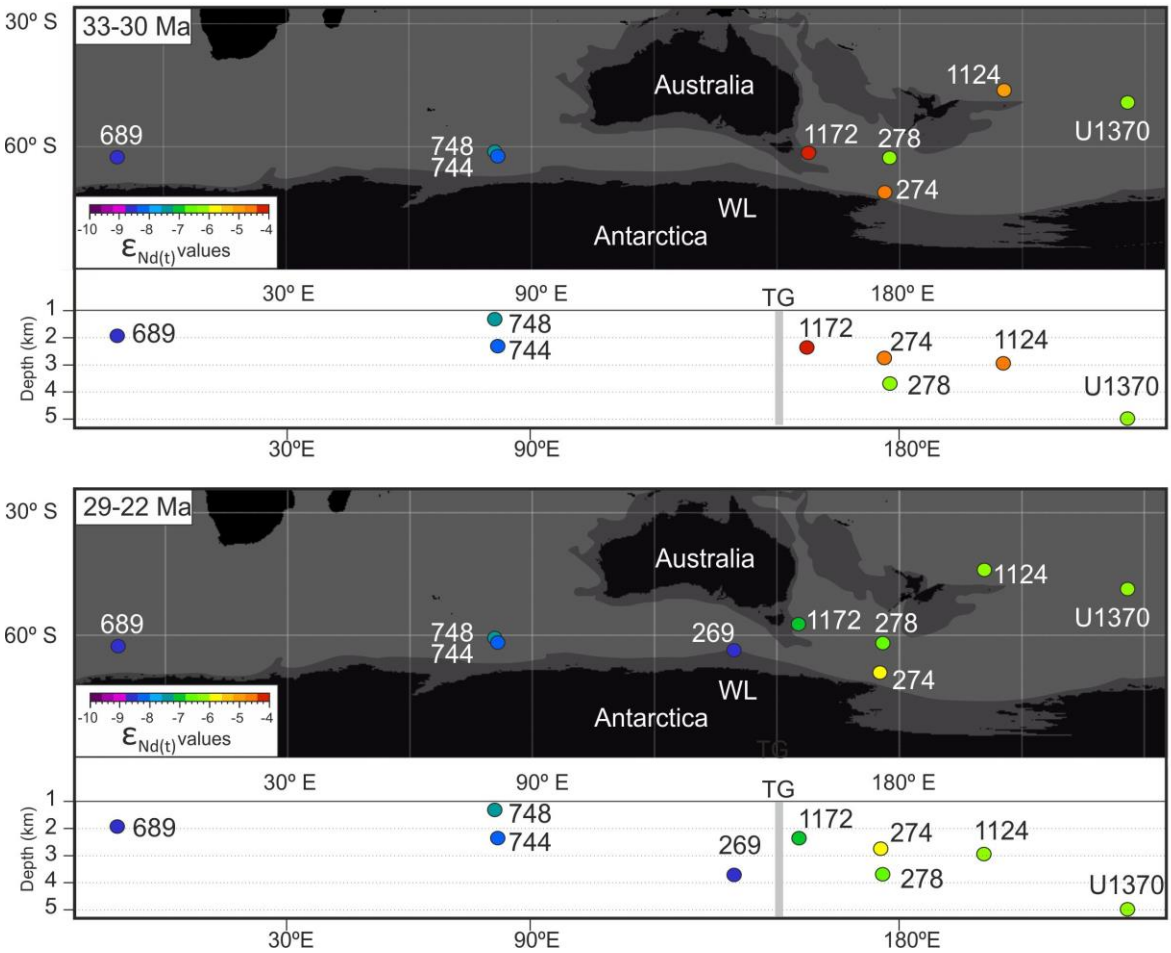

Figure 7. Map of neodymium (Nd) isotopic data discussed in the main text plotted against paleo-latitude and longitude (upper panels) and paleo-depth (lower panels) from 33 Ma to 30 Ma and from 29 to 22 Ma. Plate tectonic reconstructions and paleolocation of study Sites 278 and 274, and other sites discussed in the main text were adapted from G-plates, based on the

global plate motion model from Muller et al. (2016). Continent with present-day coastlines (black), grey boundary around continents shows areas of non-oceanic crust (e.g. continental shelves). Circles represent site locations and are coloured based on their average $\varepsilon_{Nd(t)}$ values for each period considered. Grey band indicates the position of the Tasmanian Gateway (TG).

Supplementary Information

Supplementary text

Age model for Site 278

An age-depth model for the Oligocene and lower Miocene intervals of DSDP Site 278 is developed from the integration of new magnetostratigraphic data, calcareous nannofossil, marine diatom, and radiolarian biostratigraphy, calibrated using the Geological Time Scale (GPTS) 2012 (Gradstein et al., 2012) (Fig. 3; Tables S1-S4). The initial age model prepared by the Shipboard Scientific Party on DSDP Leg 29 (Kennett et al., 1975) was of coarse resolution due in part to the infancy of diatom and radiolarian biostratigraphy. A compilation of age models from Neogene intervals of DSDP drill holes presented by Lazarus et al. (1995) included DSDP Site 278 and incorporated improved biostratigraphic age assignments as a result of 20 years of additional development and subsequent Ocean Drilling Program (ODP) drilling in the Southern Ocean during ODP Legs 113, 114, 119, and 120. These later drilling efforts included consistent integration of magnetic polarity stratigraphy in assessing the ages and correlation of biostratigraphic datum levels. The compilation of Lazarus et al. (1995) provided the general trend of age-depth for DSDP 278, but did not identify several short hiatuses of 2 – 4 m.y. duration that are resolved in our analysis. We report here the age interpretation for the time interval ~31 to ~18 Ma, and refer the reader to the report of Evangelinos et al. (in preparation) for a revised age model for the time interval < 18 Ma at DSDP Site 278.

A total of 19 samples were examined for the identification of calcareous nannofossils. Smear slides were prepared from unprocessed sediment and examined with a Leica DMRP polarizing microscope at 1000 x magnification. Occasionally, x1250 and x1600 magnification was also used for the identification of small specimens. At least 3 mm^2 (ca. 200 visual fields at x1000) were scanned to provide semi-quantitative values. To detect the presence of rare or very rare specimens an additional two to three slide traverses were observed. The nannofossil assemblages were used to define define the First and Last appearance datums (FAD and LAD) Selected calcareous nannofossil bioevents were considered in moderate to well preserved samples, Standard low to mid-latitude markers of the Martini (1971) and Okada and Bukry (1980) were absent. We instead used the high southern latitude zonations developed by Wei, 1991 and 1992; Wei and Wise (1990, 1992); Monechi and Reale (1997); Watkins and Villa (2000); Agnini et al. (2014). Biochronology was developed following Lourens et al. (2004) and Raffi et al. (2006), using astronomically calibrated ages from magnetic reversals and reference isotope stratigraphies, adjusted to the ATNTS2004 (Gradstein et al., 2004). Only 12 of these samples contained enough amounts of nannofossils to provide biostratigraphic information (Table S1). In most of these samples calcareous nannofossils are abundant. The lowest cores 278-34R to 31R consist of siliceous nannofossil chalk comprising 70 to 95% calcareous nannofossils. Diatoms increase in number at the expense of calcareous nannofossils in core 31R, and become the dominant sediment-forming microfossil in cores 30R and above. Calcareous nannofossils are present in most intervals, but their abundance drops to trace amounts or absent in some samples in cores 29R and 28R (Kennett et al., 1975).

Diatom biostratigraphic data for DSDP Site 278 were compiled from a variety of published sources, as well as new data collected for this study. Schrader (1976) provided the initial biostratigraphic characterization of 72 samples in this interval between samples 278-34R-3, 50 cm to 278-21R-1, 50 cm (his dataset continues up to core 278-9R-1, 50 cm),

reporting 58 diatom taxa in this lower interval. Weaver and Gombos (1981) compared the stratigraphy of DSDP Sites 278 and 266 in an attempt to reconcile divergent records of diatom ranges, with the resultant interpretation of a hiatus within core section 15R-2 in DSDP Site 278 that resulted in truncated ranges. Harwood (1982) examined 20 samples across the Oligocene-Miocene interval between samples 278-34R-1, 135 cm and 278-25R-2, 44 cm in the attempt to apply the diatom zonation proposed by Gombos and Ciesielski (1983) from DSDP Leg 71 in the South Atlantic to the DSDP Site 278 record, and documented the occurrence of 69 taxa. Based on the stratigraphic abundance distribution of *Rocella* spp. taxa, Harwood (1982) interpreted a hiatus between samples 278-31R-3, 139-141 cm and 278-3R1-2, 139-141 cm, which was also noted in Fenner (1984), along with the ranges of 19 other diatoms in DSDP Site 278. 35 new samples were examined by Harwood for the present study in the interval between samples 278-34R-1, 142 cm and 278-26R1, 7 cm, wherein 112 diatom taxa were noted, along with 17 other siliceous microfossil taxa (silicoflagellates, ebridians, endoskeletal dinoflagellates, and a range of unrecorded chrysophycean cysts). The diatom and other siliceous microfossil record require further documentation, as it is clear that the DSDP 278 record is an important reference section for diatom biostratigraphy. Schrader (1976) appears to have examined strewn slides from chemically-treated sediment residues, whereas Harwood (1982), following the methodology of Gombos and Ciesielski (1981), examined slides of size fractions from >37 μm and <37 μm, as well as raw strewn, chemically-treated sample residues. Similarly, in preparation for the present study, diatom samples were sieved through a smaller, 20 um mesh sieve. Sieving results in the recovery of a greater number of whole and identifiable taxa, and is responsible for the recording of numerous taxa not reported by Schrader (1976), including many marker taxa used in the Gombos and Ciesielski (1983) zonation. In addition, the recent compilation of biostratigraphic events developed for IODP Expedition 374 in the Ross Sea (McKay et al., 2019) was consulted to provide ages for diatom events noted in this

946 study. This compilation drew from output from the Constrained Analysis (CONOP) model
947 output associated with the study of ODP Site 744 as presented in Farmer (2011) and Florindo
948 et al. (2013), which builds upon the composite ordering of events and model age output for
949 Southern Ocean data sets presented by Cody et al. (2008, 2012) (Table S2).

950 Radiolarian biostratigraphic event data of first and last appearance datum levels are
951 interpreted from Table 1 of Petrushevskaya (1975). Taxon names presented in Table S3 reflect
952 those presented by Petrushevskaya, as well as names in current use. Age information and
953 taxonomic revisions are drawn from the works of Abelmann (1990), Caulet (1991), Takemura
954 (1992), and Takemura and Ling (1997), as well as from the age model output provided by the
955 CONOP analyses from ODP Site 744. Assignment of radiolarian datum events to magnetic
956 polarity chrons are drawn from the radiolarian range data of select taxa presented in Abelmann
957 (1990) from ODP Sites 689 and 690 in conjunction with age models for these sites provided
958 by Florindo and Roberts (2005).

959 In order to provide independent age constraints to biostratigraphy we studied the
960 magnetic stratigraphy of DSDP Site 278. The interpreted magnetic chrons are presented in
961 Table S4 and in Figures 3. Magnetic reversals in the samples were identified through stepwise
962 demagnetisation experiments by alternating fields (AF) using the 2G magnetometer (2G-
963 SRM750 Superconducting Rock Magnetometer) at the Paleomagnetic Laboratory of Barcelona
964 (CCiTUB-CSIC). A total of 47 samples provided reliable inclinations. Most of the samples
965 were successfully demagnetized after 80 mT, although some of them likely with higher
966 coercivity minerals were demagnetized after 120-150 mT. Core orientation is not
967 reconstructed, and magnetic inclinations are used to determine magnetic polarities (Fig. S3A)
968 In general samples depict normal and reversed polarities (Fig. S3B). We have identified 7
969 reversal events shown on Figure 3 and Supplementary Table S4.

The stratigraphic section cored at DSDP Site 278 from the bottom of the sedimentary section in core 34R at ~429 mbsf up to sample 278-21R-1, 50 cm at ~282 mbsf spans the time interval from ~ 31 to 17.7 Ma, with one unconformity noted between samples 278-31R-3, 35 cm and 278-31R-2, 139 cm (398.85 – 399.89 mbf), which removed a 2.4 m.y. time interval from 28.2 to 25.8 Ma. The top of this interval is bounded by an unconformity between samples 278-21R-1, 50 cm and 278-20R-6, 50 cm (281.5 mbsf) which removed the time interval 17.6 to 15.5 Ma.

Sediments between 396.95-428.45 mbsf (Cores 34R-31R) contain calcareous nannofossils *Reticulofenestra daviesii, Cyclicargolithus floridanus, Chiasmolithus altus, Reticulofenestra bisect/stavensis, andCyclicargolithus abisectus*. In this interval occasional reworked taxa have been observed. The interval between 379.5 and 414.41 mbsf is assigned to be between NP25 (23.13-26.84 Ma) and NP23 (29.62-32.02 Ma) due to the co-occurrence of *Chiasmolithus altus* (absent above 379.5 mbsf) and *Cyclicargolithus abisectus* (regular above 410.41 mbsf). The interval below 422.74 mbsf is attributed to an interval between biozones NP 23-NP 16?, due to the absence of *Reticulofenestra umbilicus* and the consistent presence of *Reticulofenestra bisecta/stavenis* (Martini et al.1970; Watkins and Villa, 2000; Young et al., 2017, Kulhanek et al., 2019). The LAD of diatoms *Pyxilla eocena* and *Hemiaulus rectus* var. *twista* at 422.09 and 425.43 mbsf, respectively indicate an age near 30.8 to 30.5 Ma at the bottom of DSDP 278. Recognition of the FAD of diatom *Rocella vigilans* var. A at 421.85 mbsf (30.2 Ma) and the FAD of radiolarian *Cyrtocapsella longithorax* at 417.45 mbsf (31.5 to 32.5 Ma) further constrains the age of core 33R, and allows assignment to the polarity Chrons C12n and C11n (Fig. 3; Tables S2-S4). Accordingly, the magnetic reversal at 425.44 mbsf (N1) is interpreted as the top of Chron C12n (30.59 Ma). Guided by the biostratigraphic datumsit is possible to place the base of C11n.2n and top of C11n.1n (Fig. 3, N2; Tables S4). These tie-points and derived sedimentation rate can be extended complementing the age model up to

section 31R-3, where a cluster of diatom first appearance datum levels is noted, indicating the presence of a hiatus. The FAD of diatoms '*Coscinodiscus' rhombicus* (28.45 Ma), *Azpeitia gombosi* (28.3 Ma), *Rocella gelida* (26.4 Ma) in a sample from 398.85 mbsf, the FAD of diatoms *Triceratium groningensis* (27.2 Ma) and *Rocella schraderi* (~26.3 Ma) in sample from 398.39 mbsf, and the FAD of radiolarian *Stylosphaera radiosa* (~26.0 Ma) in a sample from ~397 mbsf identify this break in time. The LAD of diatom *Rocella vigilans* (25.4 Ma) in a samplefrom 398.39 mbsf identifies when sedimentation resumed after the erosion or non-deposition associated with the hiatus (Fig. 3). Accordingly, the interval of normal polarity (N3) measured between 398.86 and 397.34 mbsf is interpreted to correlate to Chron C8n.2n (Table S4).

A major change in the sedimentation occurs in core 30R (378.91-379-75mbsf) marked by the high abundance of siliceous microfossils (Kennett et al., 1975). This interval is characterized by the presence of calcareous nannofossils *Reticulofenestra daviesii, Cyclicargolithus floridanus, Discoaster deflandrei*, while regular taxa recorded above, such as *Reticulofenestra bisecta/stavensis* and *Chiasmolithus altus* are absent. This assemblage is assigned to zone NP25 (23.13-26.48 Ma) (Martini et al., 1970; Young et al., 2017), late Oligocene; however, due to the absence of characteristic marker species in the studied samples, we cannot discard an assignment of this interval to NP25-NN1. Despite the weak and low inclinations at this interval, we tentatively assign the normal polarity zone (N4) found at 377.94 mbsf to Chron C7An, suggesting an age of 24.8 Ma. A long interval of normal polarity identified in five samples from 366.28 to 357.66 mbsf (N5; Table S4) is interpreted as correlative to Chron C7n.2n (Fig. 3). One sample of reversed polarity at 352.32 mbsf is here interpreted as Chron C6Cr.

The FAD of diatom *Raphidodiscus marylandicus* (22.7 Ma) is noted in a sample at 347.39 mbsf and *Thalassiosira spumellaroides* (22.7 Ma) in a sample at 342 mbsf. These

diatom assemblages together with the presence of the calcareous nannofossil *Cyclicargolithus floridanus* and absence of *Reticulofenestra bisecta/stavensis* and other markers recorded in the lower part of Site 278, support an assignment of this interval of DSDP 278 to be assigned to the interval to biozones NN1 (22.82-23.13 Ma) and NN2 (19-22.82 Ma) (Martini et al., 1970; Young et al., 2017; Kulhanek et al., 2019). This is consistent with the diatom record, although no precise markers were observed. The biostratigraphic constraints of cores 27R and 26R here guide the magnetostratigraphic correlation. The reversal at 337.76 mbsf (base of N7) is interpreted as the base of Subchron C6Bn.2n. Above, the reversed magnetozone is assigned to C6Bn.1r whilst the top of Chron C6Bn.1n is ascribed to the reversal occurring at 331.44 mbsf (Fig.3; Table S4). Because of the wide range provided by biostratigraphic constraints for the interval encompassing cores 29 to 26, an alternative magnetostratigraphic correlation is allowed. In such case, magnetozone N6 could correspond to Subchron C6Bn.2n and C6Bn.1n; N7 to C6An.2n; and N8 to C6An.1n. Nevertheless, we consider this correlation less likely as it implies a change in the sedimentation trend towards lower values, unlike the rest of our interpretation. In addition, the fit pattern between our local reversals and the GPTS is not as good as the one using our preferred model.

Above the polarity reversals of core 26R, there is limited chronostratigraphic control up to cores 22R and 21R where numerous diatom events are noted. The LAD of *Thalassiosira spumellaroides* (18.5 Ma) noted in a sample at 294.5 mbsf and the FAD of *Fragilariopsis pusilla* (18.5 Ma) at 286.5 mbsf indicate the age at this level. Similarly, the close association of the FAD of *Crucidenticula ikebei* (18.0 Ma) at 282.66 mbsf and the LAD of *Thalassiosira praefraga* (17.4 – 17.9 Ma) at 285.25 mbsf provides age control for this interval. Between cores 21R and 20R, we interpret the existence of a hiatus based on the coincident FADs of several diatoms in the sample at 280.01 mbsf: *Araniscus lewisianus* (17.8 Ma), *Denticulopsis*

maccollumii (16.7 Ma), *Nitzschia grossepunctata* (15.6 Ma), and radiolarian FAD of *Eucyrtidium punctatum* (17.3 Ma) in a sample at 281.60 mbsf.

Supplementary Figures

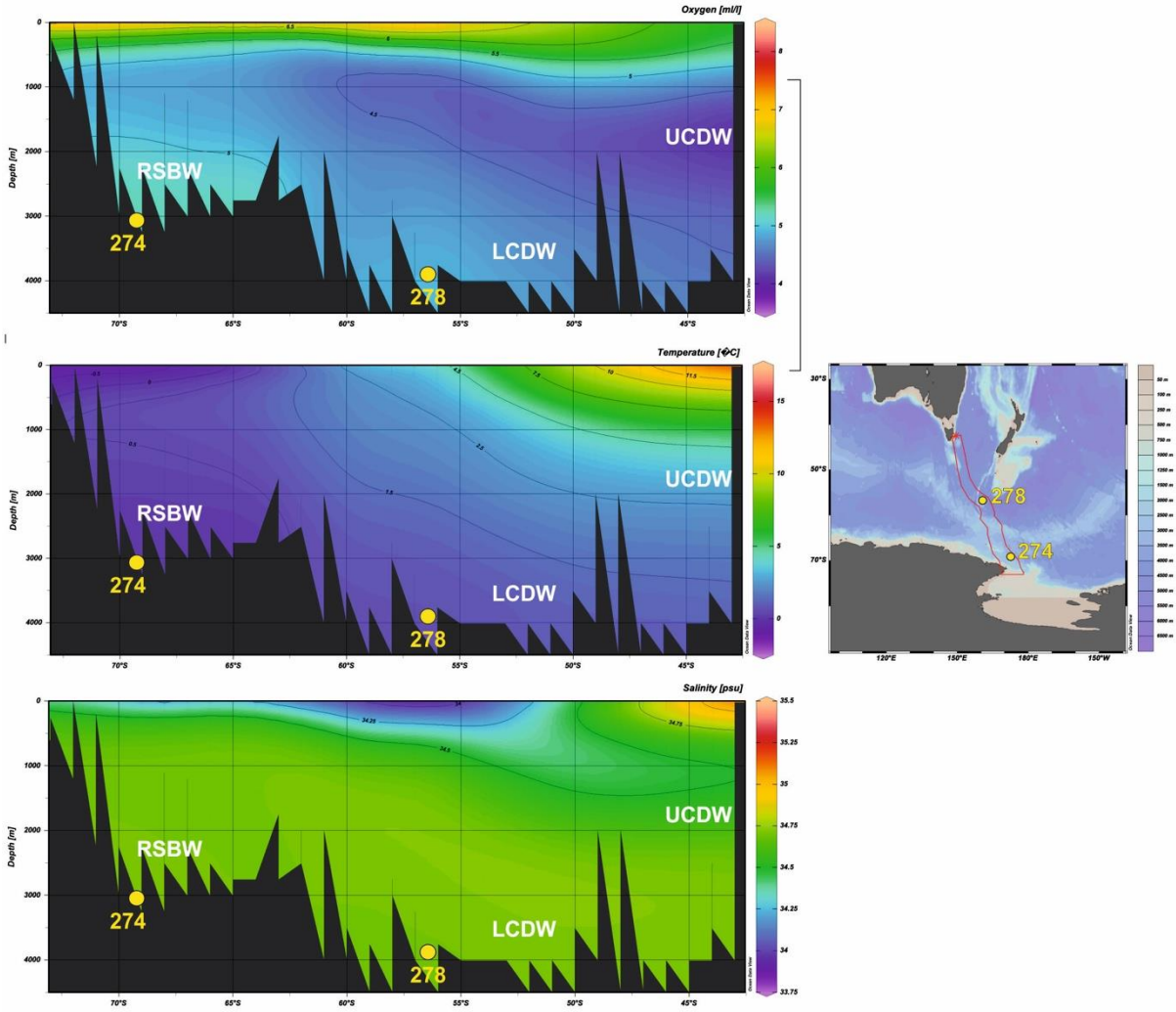

Figure S1. Maps showing the location of the sites and the distribution of dissolved oxygen, temperature and salinity versus depth along the Tasmanian to Ross Sea transect. Data derived from HYDROGRAPHIC ATLAS OF THE SOUTHERN OCEAN (Olberns et al., 1992). Maps were produced using Ocean Data View (Schlitzer, 2016). UCDW= Upper Circumpolar Deep Water; LCDW= Lower Circumpolar Deep Water; RSBW= Ross Sea Bottom Water.

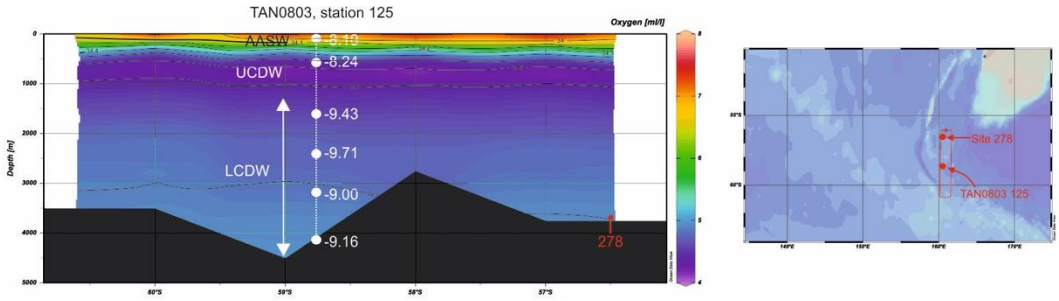

Figure S2. Neodymium isotopic composition from station TAN0803 station 125 (Lambelet et al., 2018) versus depth. Map and section were created using Ocean Data View software (Schlitzer, 2016). Antarctic Surface Water= AASW; UCDW= Upper Circumpolar Deep Water; LCDW= Lower Circumpolar Deep Water.

A) Demagnetization Diagrams (Alternating Field)

EXCLOR: dec = 183.8 inc = -66.3
int = 302 mad = 6.5

EXCLOR: dec = 192.6 inc = 41.9
int = 1038 mad = 2.1

EXCLOR: dec = 359.6 inc = -39.8
int = 119 mad = 4.4

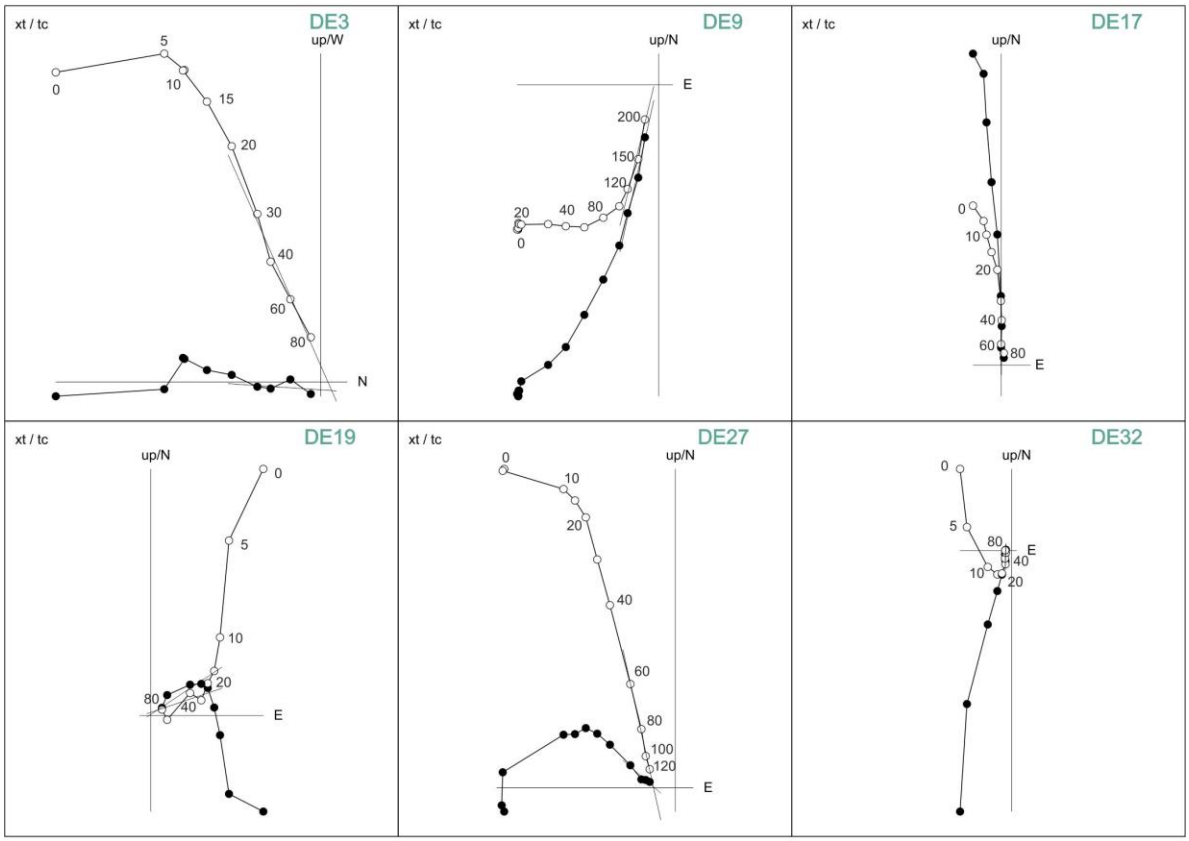

EXCLOR: dec = 56.3 inc = -15.9
int = 57 mad = 12.7

EXCLOR: dec = 311.0 inc = -73.7
int = 428 mad = 3.7

EXCLOR: dec = 181.4 inc = 45.5
int = 557 mad = 3.4

B) Distribution of Inclination

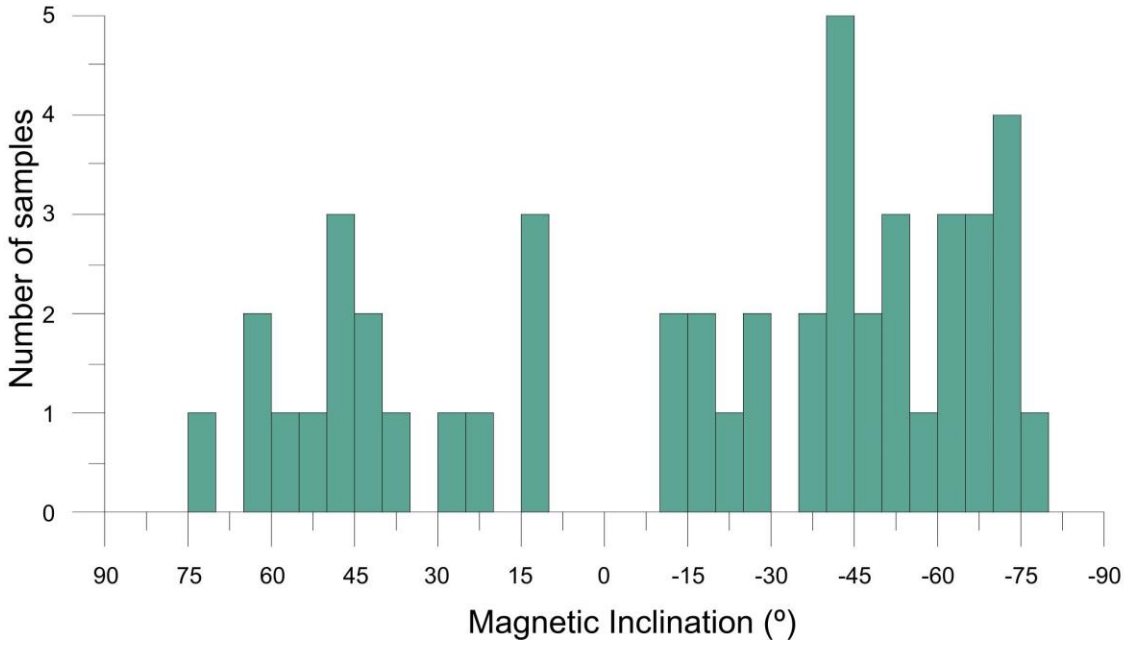

1064

1065 **Figure S3: A:** Demagnetization Diagrams **B:** Distribution of Inclination from Site 278
1066

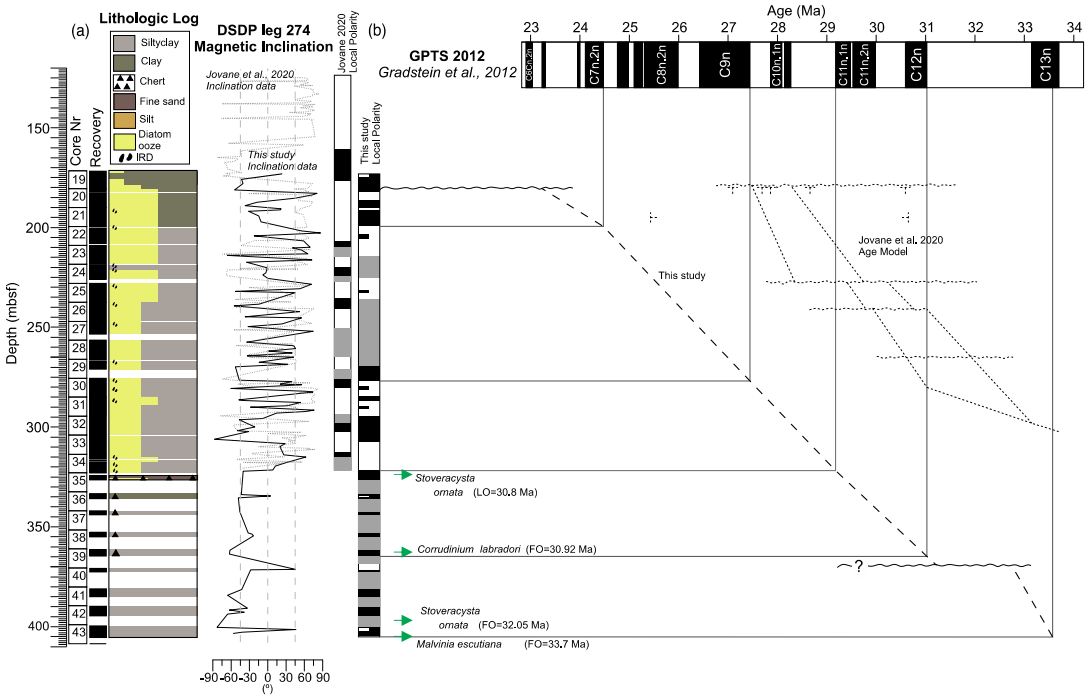

1067
1068
1069 **Figure S4.** Age mode for Site 274 from Hoem et al. (2021). (a) Core numbers, core recovery
1070 and lithologic log are based on Hayes et al. (1975). (b) Magnetic correlation for Site 274 with
1071 comparison to Jovane et al. (2020) (dotted lines). LO= Last occurrence and FO= First
1072 occurrence (see Hoem et al. (2021) for details).
1073

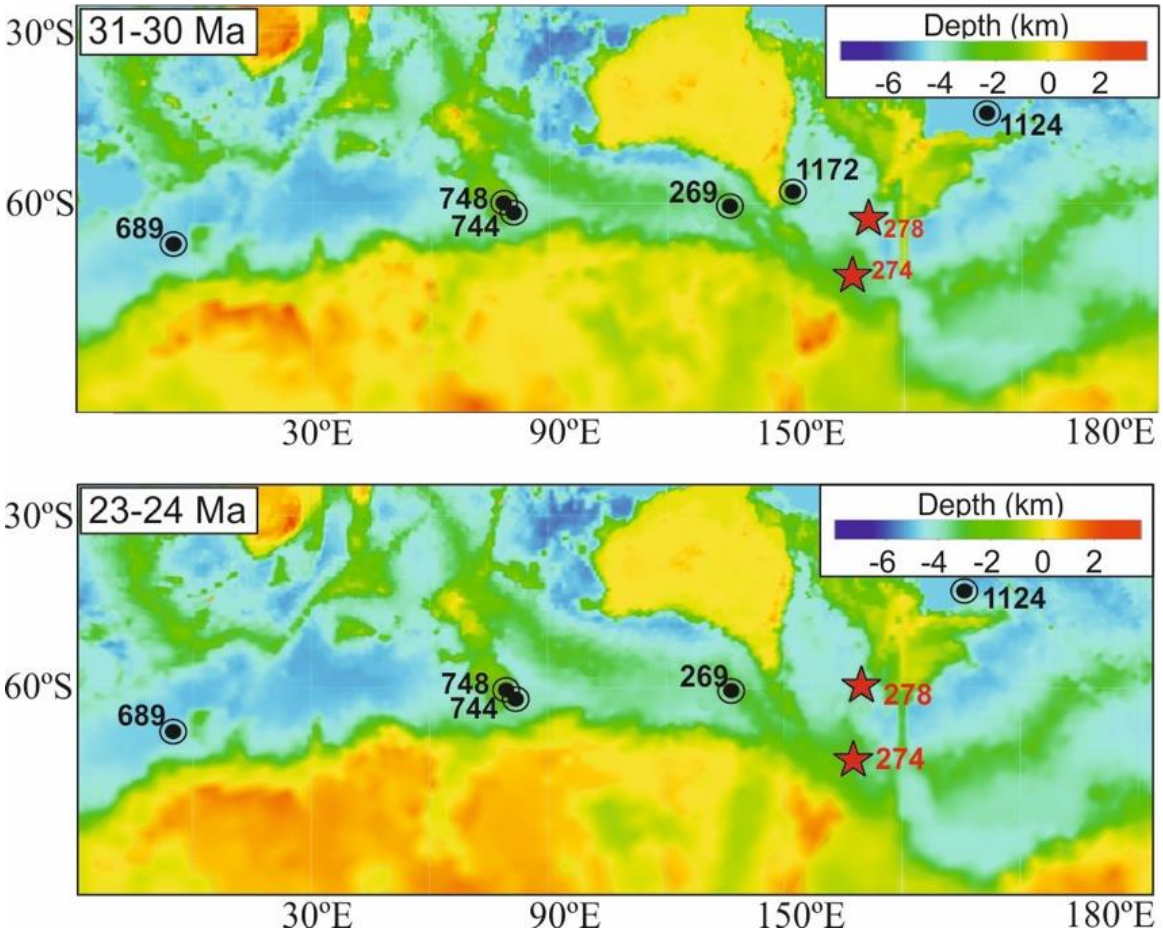

Figure S5. Paleobathymetry and paleotopography reconstructions of the Southern Ocean derived from Paleo-digital elevation model by Scotese and Wright (2018). Reconstructions of the paleolocation of study sites and sites discussed were adapted from G-plates based on Muller et al., 2016 global plate motion model.

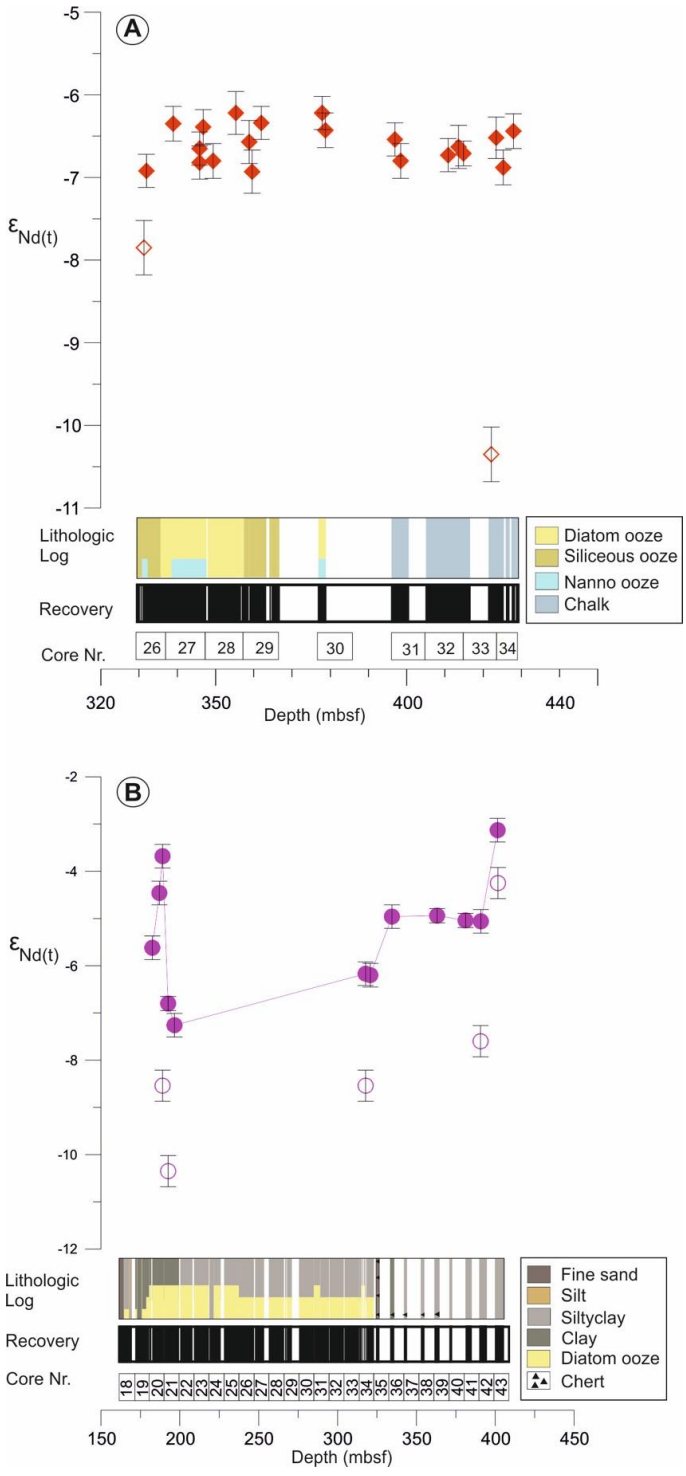

Figure S6: Neodymium isotopic composition ($\varepsilon_{Nd(t)}$) of fish debris and detrital sediment samples from this study. **A:** Fish debris $\varepsilon_{Nd(t)}$ values (red diamonds) and detrital sediment $\varepsilon_{Nd(t)}$ values (red open diamonds) at Site 278. **B:** fossil fish debris $\varepsilon_{Nd(t)}$ values (purple circles) and detrital sediment $\varepsilon_{Nd(t)}$ values (purple open circles) at Site 274.

REFERENCES for Supplementary material

Abelmann, A., 1990. Oligocene to Middle Miocene radiolarian stratigraphy of southern high latitudes from Leg 113, Sites 689 and 690, Maude Rise. In Barker, P.F., and Kennett, J.P., et al., Proceedings of the Ocean Drilling Program, Scientific Results, 113, College Station, TX (Ocean Drilling Program), 675-708.

Agnini, C., Fornaciari, E., Raffi, I., Catanzariti, R., Pälike, H., Backman, J. & Rio, D. 2014. Biozonation and biochronology of Paleogene calcareous nannofossils from low and middle latitudes. Newsletters on Stratigraphy, 47: 131–181.

Caulet, J.-P., 1991. Radiolarians from the Kerguelen Plateau. Leg 119. In: Barron, J.A., Larsen, B., et al., Proceedings of the Ocean Drilling Program, Scientific Results, 119, College Station, TX (Ocean Drilling Program), 513-546.

Cody, R.D., Levy, R.H., Harwood, D.M. and Sadler, P., 2008. *Thinking outside the zone: high-resolution quantitative diatom biochronology for Antarctic Neogene strata*. Palaeogeography, Palaeoclimatology, Palaeoecology, 260: 92-121.

Cody, R.D., Levy, R.H., Crampton, J., Naish, T., Wilson, G.S. and Harwood, D.M., 2012. Quantitative biochronology for the AND-1B drillhole. In: Wilson, G.S., Naish, T., Powell, R., Levy, R., and Crampton, J. (eds). Selection and stability of quantitative stratigraphic age models: Plio-Pleistocene glaciomarine sediments in the ANDRILL 1B drillcore, McMurdo Ice Shelf. Global & Planetary Change, 96–97 (2012) 143–156. doi:10.1016/j.gloplacha.2012.05.017

Farmer, R.K., 2011. The application of biostratigraphy and paleoecology at Southern Ocean drill sites to resolve early middle Miocene paleoclimatic events. M.S. thesis, Univ. of Nebraska-Lincoln, 65 pp., and 3 tables. https://digitalcommons.unl.edu/geoscidiss/19/

Florindo, F. and Roberts, A.P., 2005. Eocene-Oligocene magnetobiochronology of ODP Sites 689 and 690, Maud Rise, Weddell Sea, Antarctica. Geological Society of America Bulletin, 117: 46-66. doi:10.1130/B25541.1

Florindo, F., Farmer, R.K., Harwood, D.M., Cody, R.D., Levy, R., Bohaty, S.M., Carter, L., and Winkler, A., (2013). Paleomagnetism and biostratigraphy of sediments from Southern Ocean ODP Site 744 (southern Kerguelen Plateau): implications for early-to-middle Miocene climate in Antarctica. Global and Planetary Change, 110(C):434–454. https://doi.org/10.1016/j.gloplacha.2013.05.004.

Gombos, A.M., Jr. and Ciesielski, P.F., 1983, Late Eocene to early Miocene diatoms from the southwest Atlantic, In: Ludwig, W.J., Krasheninnikov, V.a., et al.,, Initial Reports of the Deep Sea Drilling Project, 71 (Pt. 2), Washington (US Government Printing Office), 583-634. doi:10.2973/dsdp.proc.71.124.1983

Gradstein, F.M., Ogg, J.G., Schmitz, M., Ogg, G., 2012. The Geologic Time Scale 2012 2-Volume Set. Elsevier.

Gradstein, F.M., Ogg, J.G., Smith, A.G., 2004. A Geologic Time Scale 2004. Cambridge University Press, Cambridge, UK.

Harwood, D.M., 1982. Oligocene-Miocene diatom biostratigraphy from the equatorial to the Antarctic Pacific. M.S. Thesis, Florida State University, Tallahassee, FL.

Jovane, L., Florindo, F., Wilson, G., de Almeida Pecchiai Saldanha Leone, S., Hassan, M. B., Rodelli, D., and Cortese, G.: Magnetostratigraphic Chronology of a Cenozoic Sequence From DSDP Site 274, Ross Sea, Antarctica, Front. Earth Sci., 8, 155–169, https://doi.org/10.3389/feart.2020.563453, 2020.

Kennett, J. P., Houtz, R.E., Andrews, P.B., et al. (1975), *Initial Reports of the Deep Sea Driling Project, 29*, 1186.

Kulhanek, D. K., Levy, R. H., Clowes, C. D., Prebble, J. G., Rodelli, D., Jovane, L., Morgans, H. E., Kraus, C., Zwingmann, H., and Griffith, E. M, 2019. Revised chronostratigraphy of DSDP Site 270 and late Oligocene to early Miocene paleoecology of the Ross Sea sector of Antarctica, Global and Planetary Change, 178, 46-64. https://doi.org/10.1016/j.gloplacha.2019.04.002.

Weaver, F.M. and Gombos, A.M., Jr., 1981. Southern high-latitude diatom biostratigrapy. In Warme, T.E., Douglas, R.G., and Winterer, E.L. (Eds.), The Deep Sea Drilling Project: A Decade of Progress. Special Publication, SEPM, 32, 445-470.

Young J.R., Bown PR., Lees J.A., (eds) (2017). Nannotax3 website. International Nannoplankton Association, 20 Jan 2017. http://www.mikrotax.org/Nannotax3.

Wei W., Wise S. W., Jr., 1990. Middle Eocene to Pleistocene calcareous nannofossils recovered by Ocean Drilling Program Leg 113 Wedell Sea. Proceedings of the Ocean Drilling Progra111, Scientific Results. 113. 639-664.

Wei W., Wise S. W., Jr., 1992. Oligocene-Pleistocene calcareous nannofossil from Southern Ocean sites 747. 748, and 751. Proceedi11gs of the Ocean Drilling Program. Scientific Results. 120. 509-522.